buildings

MDPI

Article

Enhancing Structural Resilience: Numerical Modeling of Steel Frames Filled with Concrete Block Masonry Under Cyclic Loads

Rodrigo Felipe Santos [1,*], José Carlos Lopes Ribeiro [2], Roberto Márcio da Silva [3], Leonardo Gonçalves Pedroti [2], Alba Bruna Cintra de Grandi [3], Ruan Richelly Santos [4], Ariel Miranda de Souza [2] and José Maria Franco de Carvalho [2]

1 Department of Engineering and Computing, Santa Cruz State University, Rodovia Jorge Amado, km 16, Campus Soane Nazaré de Andrade, Ilhéus 45662-900, BA, Brazil
2 Department of Civil Engineering, Universidade Federal de Viçosa, Av. Peter Henry Rolfs, Campus UFV, Viçosa 36570-900, MG, Brazil; jcarlos.ribeiro@ufv.br (J.C.L.R.); leonardo.pedroti@ufv.br (L.G.P.); ariel.souza@ufv.br (A.M.d.S.); josemaria.carvalho@ufv.br (J.M.F.d.C.)
3 Department of Structural Engineering, Universidade Federal de Minas Gerais, Av. Antônio Carlos, 6627, Pampulha, Belo Horizonte 31270-901, MG, Brazil; roberto@dees.ufmg.br (R.M.d.S.); albacdg@ufmg.br (A.B.C.d.G.)
4 Department of Structural and Geotechnical Engineering, Escola Politécnica da Universidade de São Paulo, São Paulo 05508-010, SP, Brazil; ruanrichelly@usp.br
* Correspondence: rfsantos@uesc.br

Abstract

This article presents numerical models for unbraced steel frames filled with structural masonry under cyclic loads, offering insights into their behavior and design potential. Using simplified micro-modeling in ABAQUS with the Concrete Damage Plasticity (CDP) model, the study accurately represents masonry interactions and shows strong agreement with experimental data (R^2 = 0.977). Results indicate that the fracture energy of laying joints and the friction coefficient between masonry and steel frames critically influence displacement, collapse mechanisms, and overall stiffness. Key findings reveal that the masonry infill increases frame stiffness by approximately ten times compared to the empty frame, reducing lateral deformations to less than 0.17% of the drift ratio. Masonry infills significantly enhance frame rigidity, acting as efficient bracing elements and reducing deformations, which is particularly valuable for seismic-resistant design. The research confirms the reliability of the CDP model for complex masonry behavior, validates simplified approaches for reduced computational cost, and highlights the need to incorporate friction effects in simulations. These findings provide a basis for future technical standards and offer practical strategies for engineers working with composite steel–masonry systems.

Keywords: filled steel frames; structural masonry; bracing; cyclical loads; finite element

Check for updates

Received: 10 December 2025
Revised: 25 January 2026
Accepted: 3 February 2026
Published: 14 February 2026

Copyright: © 2026 by the authors. Licensee MDPI, Basel, Switzerland. This article is an open access article distributed under the terms and conditions of the Creative Commons Attribution (CC BY) license.

1. Introduction

Masonry, a construction method utilized since ancient times, has witnessed significant evolution in construction techniques and materials. Today, it finds widespread use as a structural element in buildings or as boundary walls [1,2]. When integrated with frames, masonry forms infilled frame systems, enhancing frame stiffness and reducing lateral displacements [3–6]. It serves as a primary defense against seismic loads by dissipating energy and decreasing the fundamental vibration period [6–10]. Recent studies have indicated that vertical loading further enhances the performance of infilled frames [4,11]. Additionally, it is worth noting that openings in the masonry reduce frame stiffness, but

still result in behavior superior to unfilled frames [2,9]. While studies primarily focus on frames filled with reinforced concrete [12], investigations into panels combined with concrete [13–22], steel frames [4,6,7,11,23–29], wooden frames [30], or even as equivalent frame [31], are also present in the literature.

With the advancement in computer processing power, numerical modeling has emerged as a cost-effective tool for studying infilled frames, offering an alternative to expensive laboratory tests [4,32] including advanced damage models [33–35]. Eladly [4] developed a numerical model for steel frames filled with masonry subjected to horizontal cyclic loading and vertical static loading, considering the components of column and beam connections. The study demonstrated an increase in stiffness and a reduction in structural deformation [4].

However, there is a lack of studies that investigate the effects of different types of masonry joints and the friction coefficients at the interfaces between the blocks and the steel frame. Doudoumis [36] conducted macro-modeling of a simple infilled frame under monotonic loading, assuming linear material behavior, and analyzed various parameters relevant to the structure's behavior, finding that all parameters significantly affect the behavior of infilled frames and that the results can be extended to multi-story systems. Radnić et al. [37] performed static and dynamic numerical analyses of steel frames filled with masonry and loaded in their own plane, showing that the macro-model generated quick responses, while the micro-model achieved results equal to the experimental results but is more complex, time-consuming, and computationally demanding. Ji et al. [25] evaluated the seismic response using non-linear dynamic analysis of a masonry and steel structure building with new tuned viscous mass damper (TVMD) installations, concluding that TVMD controlled damage to structures and masonry, reducing repair time and cost. Damiani et al. [38] devised modular steel frames braced against the external surface of pre-existing brick masonry walls. They simulated in-plane lateral loading using numerical modeling grounded in the Distinct Element Method, and their findings suggest the potential for establishing standards applicable to real-world scenarios [38]. Yu et al. [6] conducted experimental shaking table tests and compared them with the numerical results of seismic evaluation using a macro-model of hinged steel frames, both with and without infill masonry. The results indicated that the numerical models could predict the dynamic behavior with reasonable accuracy and demonstrated that the presence of masonry increased the stiffness of the frame [6]. Chen et al. [39] compared experimental results of walls under blast loads with numerical simulations using simplified micro-modeling with the Riedel–Hiermaier–Thoma material model. They concluded that the numerical results provide a reference for explosive loads and that thicker and less slender walls enhance the structural performance [39]. Azandariani and Mohebkhah [29] modeled steel frames filled with masonry walls containing various door and window openings using a macro-model to evaluate their response to seismic loads. Their study yielded reliable results, showing a strong correlation with experimental data [29].

Despite the recognized advantages of integrating masonry with frames [40], this construction technique remains underrepresented in technical standards worldwide due to its complex behavior and numerous variables [2,41,42]. A bibliometric analysis conducted on the SCOPUS platform in January 2026 underscores this gap: while over 4000 works exist on the general topic of "frames and masonry", a specific filter for steel frames infilled with concrete block masonry under cyclic loads identified only 4 articles [43–46]. Most existing research focuses on reinforced concrete frames or clay brick infills, leaving a significant knowledge gap regarding the interaction between structural steel and concrete blocks in seismic scenarios. Furthermore, there is a clear scarcity of studies providing numerical analysis of concrete block masonry within steel frames.

Therefore, this research aims to evaluate the structural behavior of a steel frame filled with structural masonry under cyclic loading, providing new insights through numerical modeling. This endeavor seeks to contribute to the development of technical standards for the safe creation and control of these elements. To achieve this, a numerical model of the frame was developed using the Finite Element Method in the ABAQUS 6.12 software (Dassault Systèmes Simulia Corp., Providence, RI, USA), benchmarked against experimental results by Alvarenga [23] and De Grandi [41]. The scientific innovation lies in the specific quantification of stiffness maintenance and energy fracture for this under-researched composite system, bridging the gap between existing experimental data and practical numerical application.

2. Materials and Methods

2.1. Modeling Strategies

Modeling strategy using the Finite Element Method (FEM) was employed to assess the filled frames. FEM divides the continuous medium into finite elements, simplifying complex geometries into manageable units. This method transforms problems with infinite degrees of freedom into ones with finite degrees, easing computational resolution. However, computational resources increase with problem complexity due to the implementation of matrices, despite the method's simplification [47].

2.1.1. Masonry Modeling

The numerical analysis of masonry can be approached in two ways: through macro-modeling and micro-modeling. Micro-modeling involves the individual representation of each masonry element (blocks, mortar, and grout) and is further categorized into detailed and simplified micro-modeling. In macro-modeling, there is no distinction between materials, with masonry being represented as a composite material.

In detailed micro-modeling, all wall components are represented as continuous elements, accounting for their specific properties such as modulus of elasticity, Poisson's ratio, and relevant inelastic properties. The interface between blocks and mortar is depicted by discontinuous elements, simulating cracking/sliding planes with initial stiffness to prevent penetration of continuous elements [48].

Conversely, simplified micro-modeling condenses mortar joints and unit-mortar interfaces into a single interface, while units are enlarged to maintain the original masonry geometry (Figure 1). In this scenario, the wall is viewed as a collection of blocks connected by lines representing potential cracking or displacement at joints [14]. Although this simplification reduces processing time, it sacrifices precision by neglecting the Poisson effect of the mortar [24].

Detailed micro-modeling allows for studying the combined action of mortar, units, and interfaces, but is more suitable for smaller structures or localized phenomena due to its requirement for refined meshes and numerous material parameters, leading to longer processing times [24,49]. In simplified micro-modeling, in turn, there are shorter processing times at the cost of precision, making it preferable for larger structures where stresses can be considered uniform.

Macro-modeling treats the wall as a continuous, homogeneous, and anisotropic medium without distinguishing between individual masonry components (Figure 1d). This approach is practical for larger walls, offering simpler mesh generation, shorter processing times, and reduced memory requirements [48].

In this research, a simplified micro-model was employed to examine steel frames filled with structural masonry composed of concrete blocks. This approach was selected because it allows for the observation of failure mechanisms in the mortar joints, such as staggered

cracks, without the prohibitive computational cost associated with detailed micro-modeling of a full-scale frame.

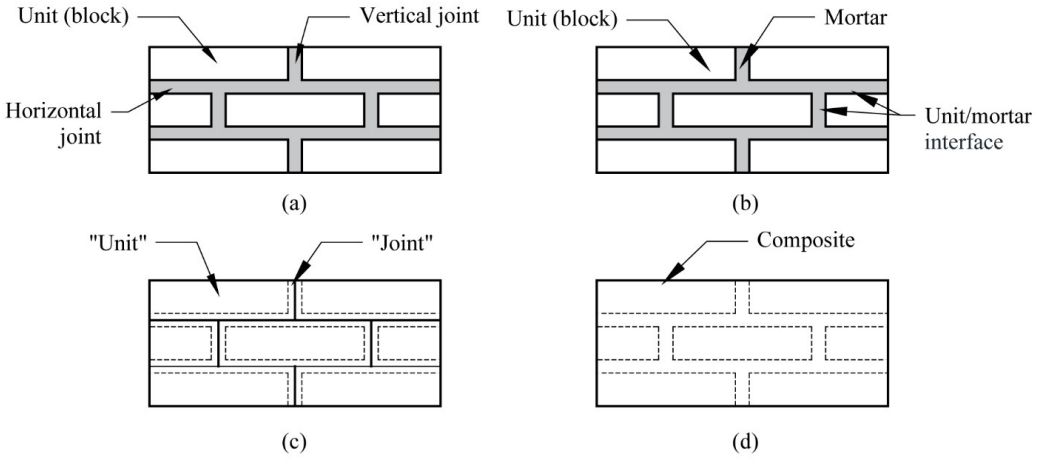


Figure 1. Masonry modeling approaches: (**a**) real masonry sample; (**b**) detailed micro-modeling; (**c**) simplified micro-modeling; (**d**) macro-modeling (adapted from Lourenço [48]).

2.1.2. Finite Element Software

There are numerous finite element software options available for modeling filled block masonry walls. Finite element analysis software offers capabilities for analyzing elements subjected to various loading conditions, including monotonic, dynamic, and cyclic loading, both in-plane and out-of-plane. Some software options are specifically tailored for seismic and explosive load analyses.

In this study, ABAQUS software was utilized, employing the Concrete Damaged Plasticity (CDP) criterion to model masonry behavior [4,50,51]. CDP, rooted in the Theory of Plasticity, accurately replicates concrete behavior under different loading conditions [52]. The mechanical problem was solved using the Newton–Raphson method, with loading applied using the "implicit" algorithm.

2.2. Geometry

The steel frame examined in this study underwent experimental testing conducted by Alvarenga [23] and De Grandi [41], with its dimensions depicted in Figure 2.

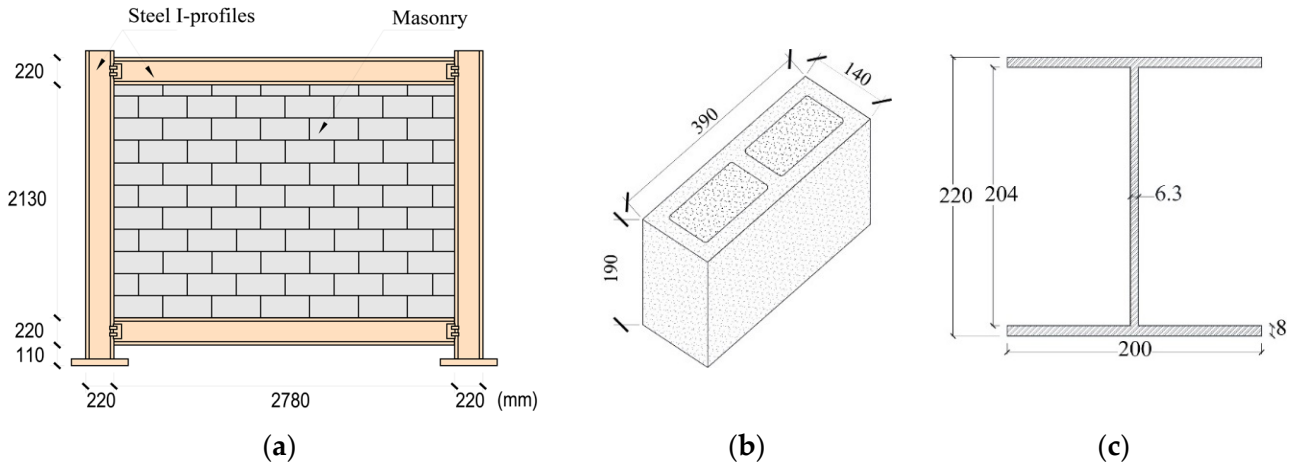


Figure 2. Geometric characteristics (**a**) of the studied steel frame, (**b**) the concrete blocks (in mm), and (**c**) of the steel I profile (in mm) adapted from Alvarenga [23].

The numerical model was developed in two stages. Initially, a model was constructed to represent the empty frame, and subsequently, the model was augmented with the inclusion of the participating masonry. Bilinear four-node quadrilateral elements were employed for the plane stress state (CPS4), which are available in the ABAQUS library. The choice to conduct a two-dimensional analysis was based on the findings of Eladly [4] and El-Khoriby et al. [53]. These authors investigated the in-plane behavior of masonry-infilled frames, achieving satisfactory results at reduced computational expense using two-dimensional models.

When modeling the empty frame, the dimension's perpendicular to the plane of the flanges corresponded to their width, while those of the webs corresponded to their thickness [4,53]. In the infilled frame model, masonry blocks were simplified as solid units with a 55.6 mm thickness, representing the average thickness of their longitudinal walls. This is justified because these walls provide the primary strength, and the block mainly acts as a stress transfer agent due to its higher strength compared to mortar. This simplification does not compromise numerical model accuracy [50].

The numerical models were calibrated based on tests conducted by De Grandi [27,41], including those for the empty frame (PV-6-CE-1.2) and the filled frame (PP-3-CE-0.5/2.0). While validated for a single-story frame, this simplified micro-modeling approach is inherently scalable and computationally efficient, allowing for the analysis of larger or irregular structures by balancing accuracy and processing time.

2.3. Interface Parameters and Connections

2.3.1. Between Blocks and Between Masonry and Steel Frame

Four properties were utilized to define the interactions between two surfaces in the model (joints), all available in the ABAQUS software: hard contact, tangential behavior, surface-based cohesive behavior, and damage. Hard contact prevents the penetration of one block into another while enabling the transmission of compression efforts. Tangential behavior replicates friction between surfaces according to Coulomb's law, requiring a static friction coefficient (μ) and a limit shear stress (τ_{max}) to trigger sliding between surfaces. For masonry, the typical friction coefficient ranges from 0.60 to 0.80, and the maximum shear stress can be determined through experimental tests. Surface-based cohesive behavior simulates the response of surfaces under tensile stresses, allowing crack propagation, akin to mortar joints in masonry. The traction-separation law in ABAQUS features a linear elastic stretch until the onset of contact damage, followed by softening, reducing normal tension (t_n) and shear (t_s, t_t) while increasing corresponding separations (δ) until total damage occurs (δ^f). The damage property enables simulation of degradation and eventual failure in cohesive surface connections through initiation and evolution processes. For damage initiation, the "maximum stress criterion" is considered, while damage evolution employs an exponential evolution, requiring the dissipated energy during failure (G^C) to be supplied [52].

Contact properties between blocks were defined based on interaction type. For tangential behavior, a friction coefficient (μ) of 0.70 and a shear stress limit (τ_{max}) of 0.2 MPa were used [41]. Cohesive behavior stiffness coefficients were k_n = 5962.26 N/mm^3 and k_s = 1035.11 N/mm^3 for horizontal joints, and k_n = 9937.09 N/mm^3 and k_s = 1725.19 N/mm^3 for vertical joints [48]. Damage onset was calculated using a maximum normal stress (t_n^0) of 1.09 MPa, equivalent to the estimated uniaxial tensile strength of the mortar (f_{te}) derived from the material's compressive strength (f_{cm}), as per Equation (1) [54]. Additionally, a maximum shear stress in the structure plane (t_s^0) of 0.2 MPa (derived from the small wall test) was adopted.

$$f_{te} = 0.3(f_{cm})^{2/3} \quad (1)$$

In the absence of experimental results, an inverse analysis was performed to determine fracture energy, adjusting values iteratively [41].

Figure 3a illustrates the friction criterion constrained by a critical shear stress. Figure 3b depicts the cohesion criteria on surfaces subjected to separation.

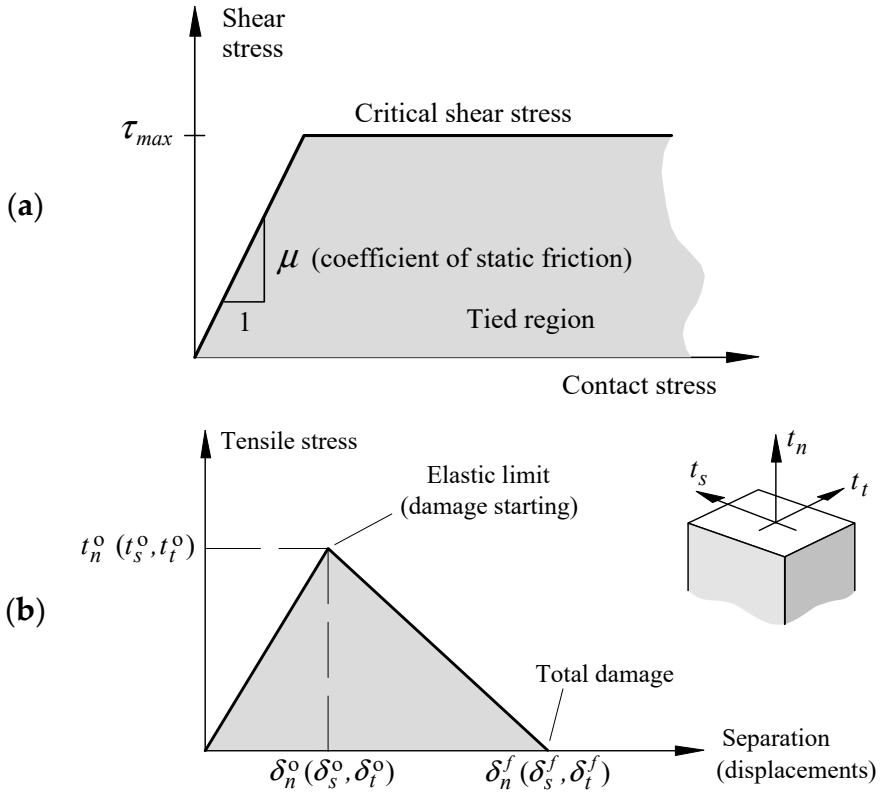
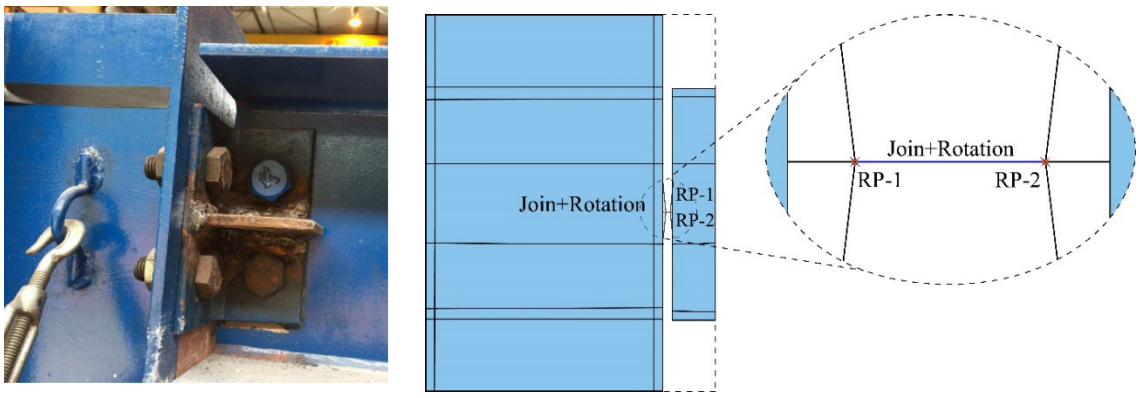


Figure 3. Criteria of (**a**) friction limited by a critical shear stress, and (**b**) cohesion at surfaces subject to separation (adapted from Simulia [52]).

Only hard contact and tangential behavior were considered between the masonry and steel frame, with a friction coefficient (μ) of 0.25 [11,55,56]. Later, friction was disregarded to assess its impact on the numerical results. This analysis was performed because some studies suggest minimal influence of friction between the panel and the steel, with some researchers omitting this parameter in their analyses [4,57].

2.3.2. Between the Beams and Columns

A labeled connection approach was implemented between the beams and columns to ensure more consistent results [58]. To achieve this, a Coupling type constraint was utilized between the column region expected to be in contact with the connecting angle and a designated reference point external to the column (RP-1). Similarly, the same procedure was applied to the beam using another reference point (RP-2). Subsequently, a Join + Rotation connector (see Figure 4) was established between the two reference points. The Join property facilitated the linkage of all translations between the two reference points, while the Rotation property specifically linked rotations around the x and y axes, simulating the effect of a hinge around the z-axis. The rotational strength (elastic constant) adopted was approximately zero (10^{-20} N.mm).

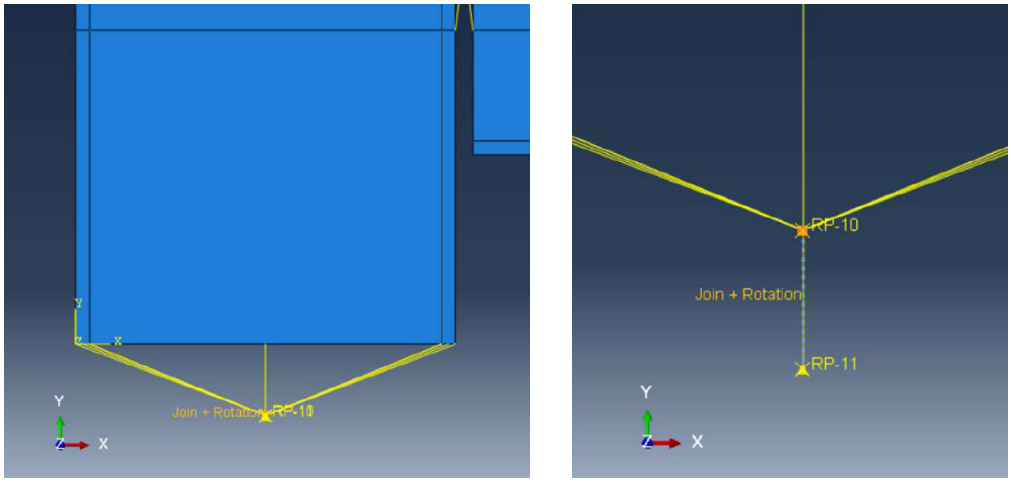


(**a**) (**b**)

Figure 4. Connection between the steel I-profiles of the frame: (**a**) experimental and (**b**) numerical.

2.3.3. Connection at the Columns' Base

The connection at the columns' base was deemed semi-rigid, as indicated by the displacement transducers used in the frame tests, which detected slight movement at the base screws [41]. The modeling was similar to the connection made between the beams and columns. The nodes of the column base were coupled to a reference point (RP10), and another reference point (RP11) was created and embedded to serve as support for the structure. Finally, the two points were joined with a Join + Rotation connector (Figure 5).



(**a**) (**b**)

Figure 5. Semi-rigid connection of the pillar base using the Join + Rotation connector: (**a**) overall view of the connection model; (**b**) enlarged detail highlighting the connection region for improved visualization.

An elastic constant for rotation around the *z*-axis was calibrated from the empty frame test results, resulting in a value of 2.0×10^{10} N.mm.

2.4. Constitutive Models of Materials

2.4.1. Steel

The stress–strain curve for steel elements proposed by Byfield and Dhanalakshimi [59] was applied, along with the von Mises flow criterion. Table 1 outlines the parameters utilized. Within the ABAQUS software, the curve was integrated by converting the engineering stress to true stress (Cauchy).

Table 1. Parameters of the steel stress–strain curve.

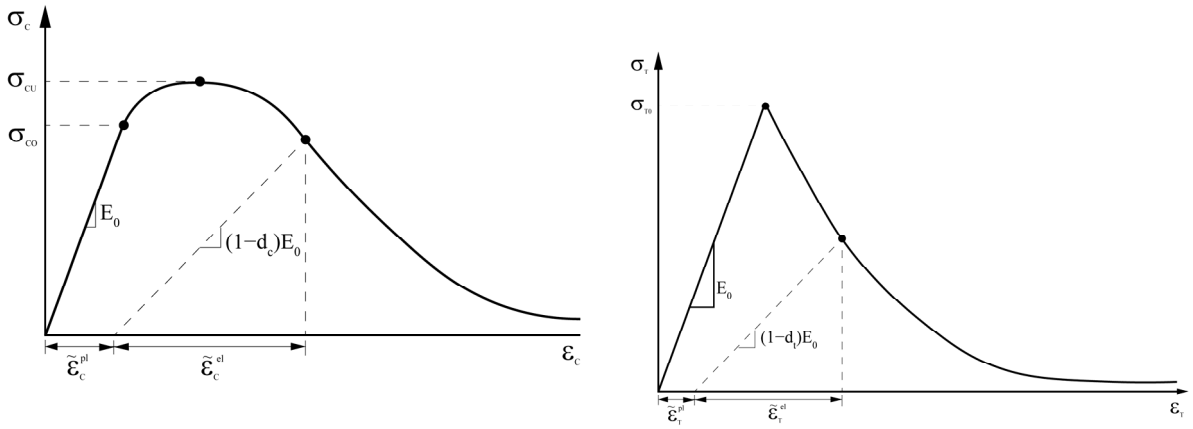
Steel	v	E (GPa)	E_{sh} (GPa)	f_y (MPa)	f_u (MPa)	ε_y (‰)	ε_{sh} (‰)	ε_u (‰)
ASTM A36	0.30	200	2.70	250	400	1.25	7.5	63.06

Note: v = Poisson's ratio; E = longitudinal elastic modulus; E_{sh} = hardening module; f_y = uniaxial tensile strength limit; f_u = ultimate tensile strength limit; ε_y = specific flow deformation; ε_{sh} = specific hardening deformation; ε_u = specific rupture deformation.

2.4.2. Concrete

Different constitutive models represent masonry behavior, including the Concrete Damaged Plasticity (CDP) model, available in ABAQUS. CDP is based on Plasticity Theory and simulates concrete under monotonic, cyclic, and dynamic loading at low confining pressures. It accounts for failure mechanisms like tensile rupture and compressive crushing [52].

In uniaxial compression (Figure 6a), concrete follows a linear stress–strain response until the initial plasticization stress (σ_{c0}), then strengthens until the ultimate stress (σ_{cu}) before degrading. Stiffness degradation is quantified by d_c damage, ranging from 0 (undamaged) to 1 (fully damaged) [52].



(**a**) (**b**)

Figure 6. Graph of concrete stress–strain under uniaxial (**a**) compression and (**b**) tension (adapted from Simulia [52]).

The mechanical problem was solved using the Newton–Raphson method, with loading applied using the "implicit" algorithm. The concrete compression was modeled using the stress–strain curve proposed by Guo [60], as outlined in Table 2. The behavior of concrete under uniaxial tension in CDP is illustrated in Figure 6b, where concrete shows linear behavior until reaching the ultimate tensile stress (σ_{t0}). Beyond this point, microcracks form, leading to a loss of strength capacity [61]. Damage d_t represents this degradation, influenced by temperature, plastic deformations, and other variables.

Table 2. Masonry compression curve parameters.

f_{cm} (MPa)	E_0 (MPa)	E_p (MPa)	$\varepsilon_{40\%}$ (m/m)	ε_p (m/m)	α_a	α_d
5.50	6500	2750	0.00034	0.0020	2.36	0.40

Note: f_{cm} = concrete compressive strength limit; E_0 = modulus of elasticity at 40% of the compressive strength of concrete; E_p = secant elasticity modulus corresponding to the compressive strength of concrete; $\varepsilon_{40\%}$ = specific deformation at 40% of the compressive strength of concrete; ε_p = specific deformation corresponding to the compressive strength of concrete; α_a = ratio between the elastic modules E_0 and E_p; α_d = parameter of the post-peak branch of the Guo curve [60].

To model the tensile strength in ABAQUS, the crack opening criterion is used, with fracture energy (G_F) being a key parameter. Hordijk's cracking–stress curve [62] is employed for the concrete blocks, with the parameters detailed in Table 3.

Table 3. Parameters of the masonry cracking–stress curve.

f_{te} (MPa)	c_1	c_2	G_F (N/mm)	w_c (mm)
0.93	3.00	6.93	0.099	0.546

Note: f_{te} = concrete tensile strength limit; c_1 = Hordijk curve parameter [62]; c_2 = Hordijk curve parameter [62]; G_F = concrete fracture energy to traction; w_c = characteristic value of crack opening.

The Hordijk [62] model considers an exponential behavior of the post-peak phase, governed by Equation (2), where f_{te} is the average tensile strength of concrete; w is the crack opening; w_c is the characteristic value of crack opening; c_1 and c_2 are constants defined by Hordijk [62]: $c_1 = 3$ and $c_2 = 6.93$. The tensile strength (f_{te}) for the prism was estimated using Equation (2).

$$\sigma_{ct} = f_{te}\left\{\left[1 + \left(c_1\frac{w}{w_c}\right)^3\right]exp\left(-c_2\frac{w}{w_c}\right) - \frac{w}{w_c}\left(1 - c_1^3\right)exp(-c_2)\right\} \quad (2)$$

The characteristic value of crack opening is given by Equation (3), where G_F is the fracture energy, calculated according to FIB [63], using Equation (4), as a function of the average compressive strength of the concrete.

$$w_c = \frac{5.14\ G_F}{f_{te}} \quad (3)$$

$$G_F = 73\ f_{cm}^{0.18} \quad (4)$$

The concrete compressive strength (f_{cm}) was derived from the prism test conducted by De Grandi [41]. However, the test to determine the modulus of elasticity of the block and prism (E_0) was not performed, and it was necessary as CDP parameter. Hence, this parameter was obtained through inverse analysis based on the initial loading cycles of the infilled frame, corresponding to the elastic behavior phase. Values ranging from 5000 MPa to 9000 MPa were tested, with 6500 MPa yielding the most favorable results, exhibiting deviations from experimental data less than or equal to 10%.

For loading beyond the peak compressive (f_{cm}) and tensile (f_{te}) strengths, the concrete's modulus of elasticity is adjusted based on two independent variables: d_c (compressive damage) and d_t (tensile damage). These variables range from zero (indicating non-damaged material) to one (representing 100% damaged material), as determined by Equations (5) and (6) [49]. In the equations, σ_c represents the compression stress, and σ_t represents the tensile stress at the specific point of the curve.

$$d_c = 1 - \frac{\sigma_c}{f_{cm}} \quad (5)$$

$$d_t = 1 - \frac{\sigma_t}{f_{ctm}} \quad (6)$$

For concrete masonry elements of this work, the analysis utilized the CDP model parameters detailed in Table 4.

Table 4. CDP model parameters (masonry elements).

Elastic Region		Plastic Region				
E (MPa)	v	ψ (°)	ε	σ_{b0}/σ_{c0}	K	μ
6410.18	0.20	32	0.10	1.16	0.6667	0.001

Note: E = longitudinal elastic modulus; v = Poisson's ratio; ψ = expansion angle; ε = eccentricity of the flow criterion; σ_{b0}/σ_{c0} = relation between resistance to biaxial and uniaxial compression; K = flow surface form factor (0.6667 for the Mohr-Coulomb criterion); μ = viscosity.

2.5. Loading Application and Force-Displacement Wraps

As in De Grandi's [41] experiment, a cyclic loading with progressively increasing intensity was applied to the numerical model, as depicted in Figure 7.

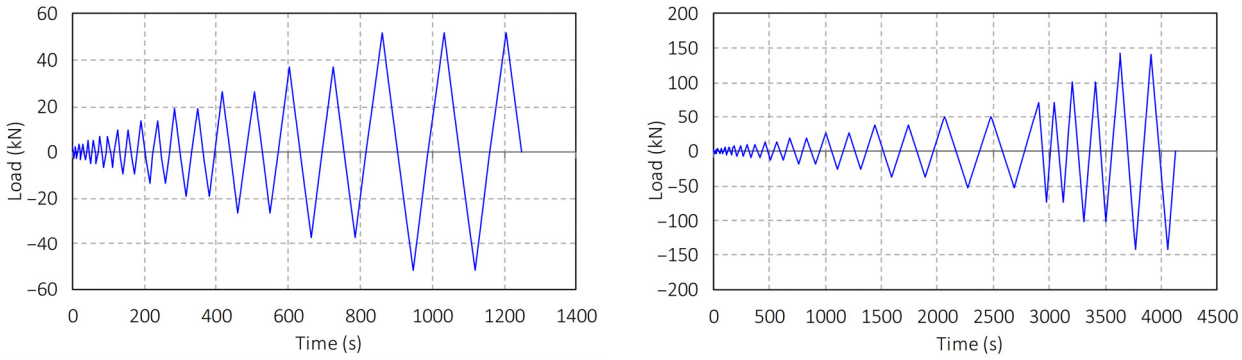


Figure 7. Load applied to the numerical model of (**a**) empty frame and (**b**) infilled frame.

The loading history of the frames was based on the specifications of the Federal Emergency Management Agency (FEMA 461:2007) [64]. For the empty frame, 10 load increments were adopted, with the first increment (a_1) being 2.5 kN. The remaining cycles followed Equation (7). In addition, two cycles were performed for each amplitude and the load application speed was 1.2 kN/s.

$$a_{i+1} = 1,4\ a_i \tag{7}$$

The loading of the filled frame was carried out with the same load as the previous one, that is, it started with a load of 2.5 kN and the increments followed Equation (7). The load application speed was 0.5 kN/s up to a load of 51.7 kN, and from then on, the speed became 2 kN/s until reaching the final load of 142 kN.

To facilitate load application and subsequent data reading, a kinematic coupling was created between the column nodes (the region of the frame in contact with the hydraulic actuator in the test) and a reference point (RP13), as shown in Figure 8. In the numerical model, the force applied at the reference point is automatically distributed to the corresponding area of the column.

In analyzing the results, the focus was on the most critical scenario where the load exerted is at its maximum, considering both stability and strength of the structure. Thus, the envelope of the force-displacement curve served as a suitable approach to characterize the behavior of frames, whether empty or filled. This methodology, adopted in the works of Bolhassani et al. [51] and Faleschini et al. [65] for concrete structures under cyclic loading, involves constructing envelopes with the maximum points from the force-displacement hysteresis curve of the structure, encompassing the peak points of the first cycle of each loading step. In this study, a slight deviation from this approach was made: for the first loading step of the infilled frames, the peak of the second cycle was considered to

accommodate the initial interaction between the masonry elements and between the panel and the frame.

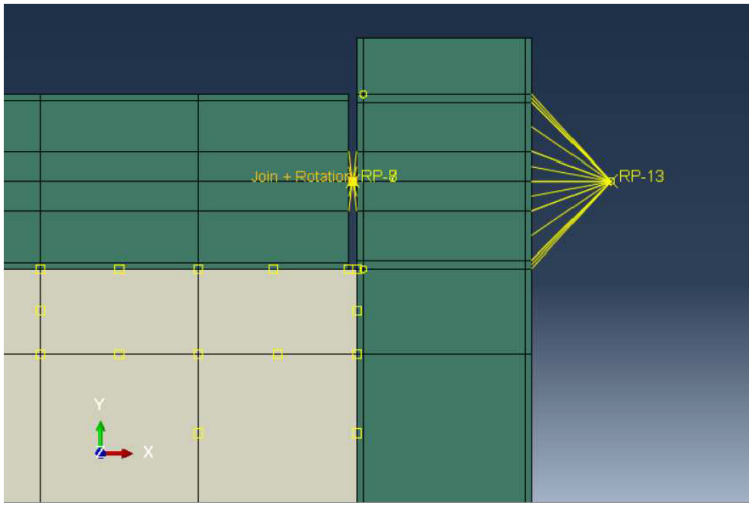


Figure 8. Kinematic coupling adopted for load application.

2.6. Finite Element Mesh

To generate the mesh of the frame and blocks, the four-node quadrilateral bilinear element of the plane stress state (CPS4) from the ABAQUS library was used (Figure 9). This element has four integration points and two translational degrees of freedom per node.

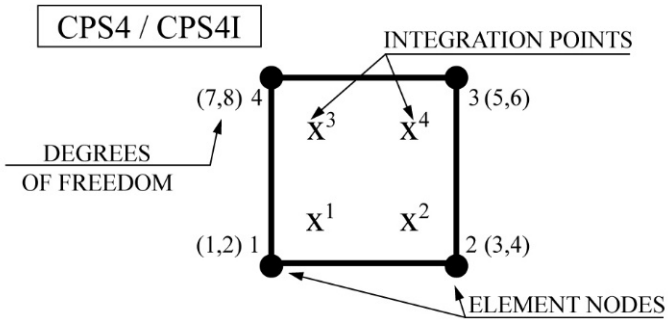
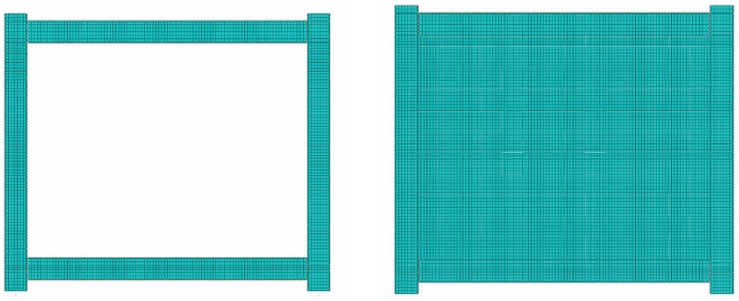


Figure 9. Diagram of the CPS4 element (adapted from Kawecki and Podgórski [66]).

After constructing the geometry of the models, assigning the material characteristics, boundary conditions, and loading, a mesh refinement test was conducted, verifying mesh sizes of 10, 20, 30, 40, and 50 mm edges. Considering the force-displacement envelopes of the empty and filled frames, the masonry collapse modes, and the processing time, it was decided to use a maximum mesh size of 30 mm for the ABAQUS mesh generator in this work (Figure 10).



(**a**) (**b**)

Figure 10. Finite element mesh of the models: (**a**) empty frame and (**b**) infilled frame.

3. Results and Discussion

3.1. Numerical Results for the Empty Frame

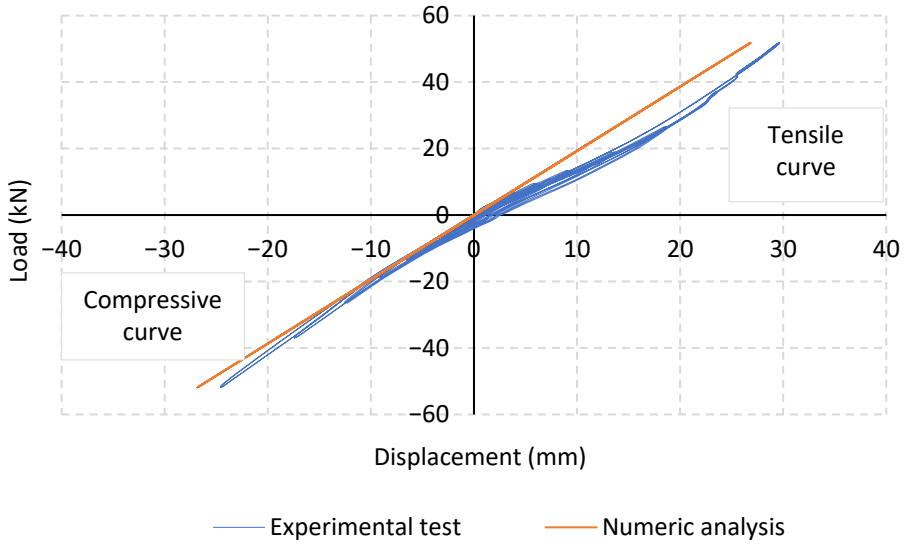
Figure 11a illustrates the numerical and experimental findings for the empty frame. The numerical model displays an elastic-linear behavior, consistent with the controlled loading during testing, which prevented the steel I-profiles from reaching plastic deformation. However, the experimental results show hysteresis in the structural system with a slight degree of plasticization. Although the maximum load was limited to avoid plasticization of the empty frame, some mechanisms may have produced the observed phenomenon: (i) residual stresses generated in the manufacturing process of the steel profiles; (ii) the use of the frame in previous load tests, which may have resulted in the plasticization of portions of the structure; and (iii) accumulation of stresses in some connection regions.

Another fact that may have been relevant to the observed behavior was the performance of the bolted angle plates used in the experimental test. During the tests, it was necessary to reinforce such parts to limit their deformations during the force acting in the positive direction (Figure 11b) corresponding to the tensile curve [41]. When analyzing the graph in Figure 11a, it seems that even the adoption of reinforcement was not enough to eliminate the differential behavior of the angle plate in relation to the directions of the applied loads. The experimental data on the difference in performance of the angle plates as a function of the load direction were not collected in the test. Therefore, it was not possible to use them as parameters in the numerical model. The solution found was to develop a model that simulated behavior closer to the theoretical one, with the angle plates acting similarly in compression and tension, which was to be expected. Despite the differences observed, mainly in the tensile curve, the numerical model was able to reproduce the results of the compression curve well. And in the infilled frame model, it was able to accurately estimate the beginning of the failure of the infill masonry, both the load at which the damage occurred and the type of damage observed, as will be demonstrated in the next item.

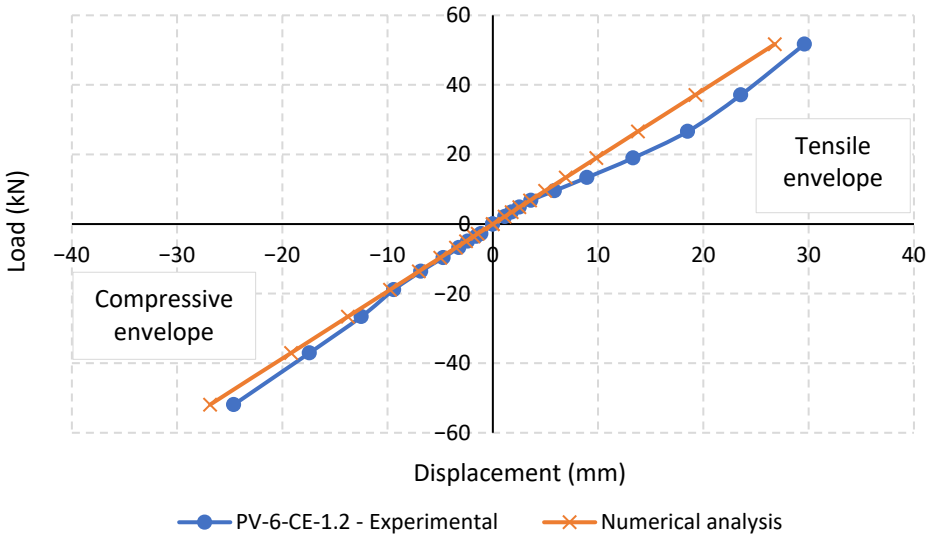
Figure 11b displays the experimental and numerical envelopes, as per the method outlined by Faleschini et al. [65]. While the experimental results for the tensioned bracing exhibit non-linearity, there is a general correlation between the envelopes.

To assess alignment between numerical and experimental envelopes, the coefficient of determination (R^2) was calculated. The analysis was based on the values in Table 5, which were also used to construct the envelopes in Figure 11b. Numerical values, derived from principles of Strength of Materials, Theory of Elasticity, and Theory of Plasticity, were treated as theoretical constructs. Experimental values, subject to variability across experiments, were considered empirical samples. The experimental protocol entailed controlled load application and displacement measurement, with force as the independent variable and displacement as the dependent variable. For the drift ratio calculation (Figure 11c), a height of 2570 mm was considered, corresponding to the distance between the base of the frame and the point of load application (point RP in Figure 8).

(**a**)



(**b**)



(**c**)

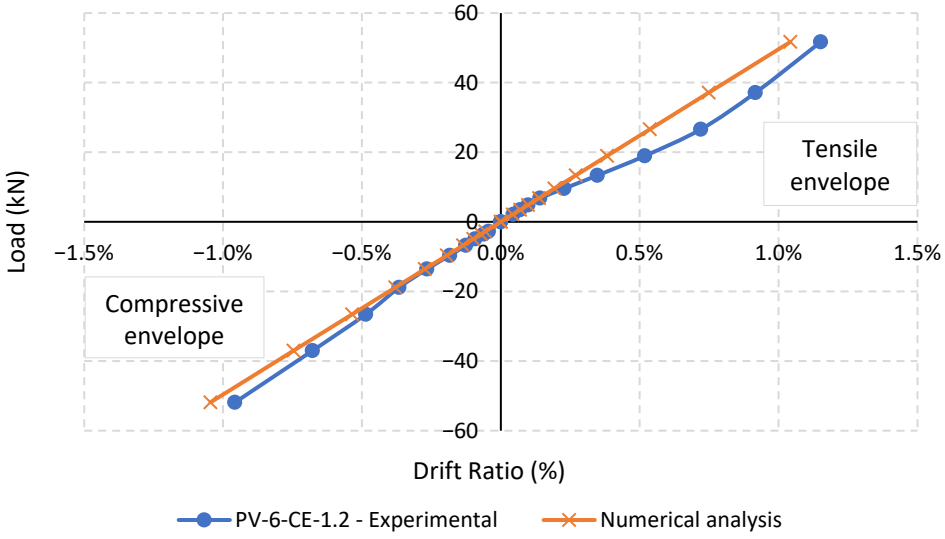
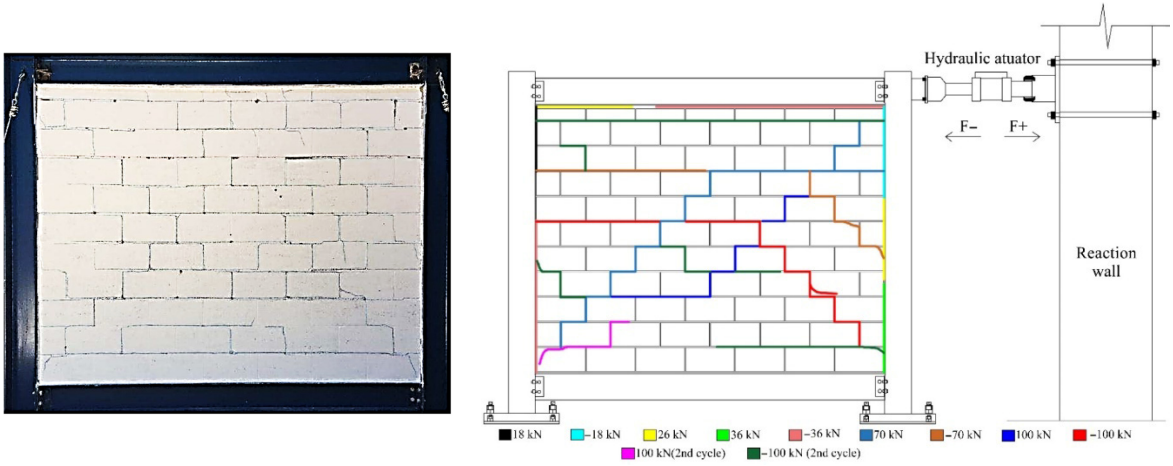


Figure 11. Comparison between (**a**) experimental and numerical results, (**b**) experimental and numerical envelopes, and (**c**) experimental and numerical drift ratios (empty frame). Note: The abscissa represents the displacements at the top of the frame (corresponding to point RP-13 in the numerical

model), while the ordinate corresponds to the loads applied to the frame. The sign convention for force and displacement follows the scheme illustrated in Figure 12. In Figure 11b, each '×' and '•' symbol represents the peak load–displacement point of the first cycle for each load step.



(**a**) (**b**)

Figure 12. Cracks in the infilled frame PP-3-CE-0.5/2.0 in (**a**) the real image and (**b**) an illustration with cracks colored according to the breaking force (adapted from De Grandi [41]).

Table 5. Results obtained experimentally and numerically at each loading step (empty frame).

Part of Envelope	Load Step	Time (s)	Load (kN)	Displacement (mm)		Drift Ratio (%)		Relative Deviation (%)	Displacement in the Numerical Model
				Experimental	Numerical	Experimental	Numerical		
Compressive	0	0	0	0	0	0.00%	0.00%	0	Equal
	1	4	−2.76	−1.12	−1.43	−0.04%	−0.06%	28.19	Bigger
	2	23	−3.54	−1.55	−1.83	−0.06%	−0.07%	18.21	Bigger
	3	50	−4.91	−2.37	−2.54	−0.09%	−0.10%	7.45	Bigger
	4	87.5	−6.76	−3.22	−3.50	−0.13%	−0.14%	8.60	Bigger
	5	140.5	−9.64	−4.71	−4.99	−0.18%	−0.19%	6.09	Bigger
	6	214	−13.57	−6.83	−7.03	−0.27%	−0.27%	2.85	Bigger
	7	317	−18.85	−9.40	−9.76	−0.37%	−0.38%	3.89	Bigger
	8	461	−26.57	−12.49	−13.76	−0.49%	−0.54%	10.17	Bigger
	9	663.5	−37.01	−17.42	−19.17	−0.68%	−0.75%	10.07	Bigger
	10	946.5	−51.86	−24.60	−26.86	−0.96%	−1.05%	9.20	Bigger
Tensile	0	0	0	0	0	0.00%	0.00%	0	Equal
	1	8.5	2.16	1.15	1.12	0.04%	0.04%	2.55	Smaller
	2	17.5	3.45	1.79	1.79	0.07%	0.07%	0.10	Equal
	3	42.0	4.87	2.54	2.52	0.10%	0.10%	0.61	Smaller
	4	76.0	6.83	3.63	3.54	0.14%	0.14%	2.61	Smaller
	5	124.5	9.59	5.87	4.97	0.23%	0.19%	15.37	Smaller
	6	191.5	13.38	8.95	6.93	0.35%	0.27%	22.52	Smaller
	7	285.5	18.99	13.33	9.84	0.52%	0.38%	26.21	Smaller
	8	417.0	26.62	18.51	13.79	0.72%	0.54%	25.49	Smaller
	9	602.0	37.14	23.57	19.24	0.92%	0.75%	18.40	Smaller
	10	860.5	51.72	29.61	26.79	1.15%	1.04%	9.53	Smaller

To calculate the coefficient of determination, Equation (8) was used, where TSS is the total sum of squares, representing the total variability of the dependent variable, that is, the displacement. It is obtained by adding the squares of the differences between the mean of the observations ($\overline{y}$) and the observed value (y_i), according Equation (9). In the analysis in question, this mean and the observed values correspond to the experimental ones.

$$R^2 = \frac{ESS}{TSS} = 1 - \frac{RSS}{\text{TSS}} \tag{8}$$

$$TSS = \sum_{i=1}^{n} (y_i - \overline{y})^2 \tag{9}$$

ESS is the explained sum of squares, representing the variability of the dependent variable (displacement) that is explained by the independent variable (force). It is obtained by adding the squares of the differences between the estimated values ($\hat{y}_i$), that is, the numerical data, and the mean of the experimental observations ($\overline{y}$), according to Equation (10).

$$ESS = \sum_{i=1}^{n} (\hat{y}_i - \overline{y})^2 \quad (10)$$

RSS is the residual sum of squares, representing the variability of the dependent variable that is not explained by the independent variable. It is obtained by adding the squares of the differences between the experimentally observed values (y_i) and the numerically estimated values ($\hat{y}_i$), according to Equation (11).

$$RSS = \sum_{i=1}^{n} (y_i - \hat{y}_i)^2 \quad (11)$$

By calculating Equations (9) and (11) and substituting them into Equation (8), the coefficient of determination (R^2) was obtained as 0.977. Since this value is very close to 1, it was concluded that the numerical data explain the experimental envelope very well.

3.2. Numerical Results for the Infilled Frame

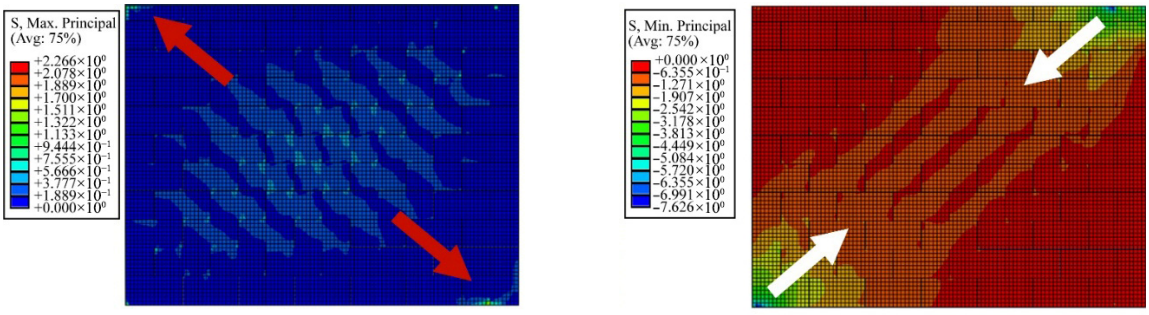
The fracture energies for both vertical and horizontal mortar joints in the numerical simulation were derived via inverse analysis, utilizing experimental data from De Grandi [41].

Observations revealed that lower adopted energies led to premature separation between masonry blocks in the numerical model. Conversely, higher values impeded joint separations for the anticipated loads in the tests. Consequently, iterative searches were conducted to identify fracture energy values that accurately replicated the observed cracking pattern in the experiment.

In the adjusted numerical model, denoted as PP-E415-050Exp, a fracture energy of 4.15 N/mm was applied to horizontal joints and 0.50 N/mm to vertical joints, incorporating exponential damage evolution. This model successfully predicted the initiation of the first crack in the masonry.

In the PP-3-CE-0.5/2.0 frame test conducted by De Grandi [41] (depicted in Figure 12), initial cracks manifested at the interfaces between the steel frame and the masonry, particularly in the tensioned corners, consistent with literature descriptions [2,3,42,67]. Within the masonry, the first discernible crack emerged under a load of 70 kN when the hydraulic actuator displaced the frame to the right. This condition induced separation of the horizontal joint at the masonry's apex, along with staggered cracks in the rightward region, extending to some blocks. Conversely, when the hydraulic actuator shifted the frame leftward under a 70 kN load, a similar yet mirrored crack pattern ensued. Subsequently, under a 100 kN load, additional cracks emerged, mirroring the separation pattern observed in the horizontal joints, featuring both staggered and block-bound cracks.

In the numerical model, prior to reaching the 70 kN load threshold, which signifies the onset of mortar joint separation, a distinct pattern emerges. This pattern includes the formation of compression rods and regions experiencing greater tensile stress (tensile rods), as depicted in Figure 13.



(**a**) (**b**)

Figure 13. Displacement of the frame to the left with the formation of (**a**) tension struts (σ_{max}) and (**b**) compression struts (σ_{min}) (displacement magnification: 1×).

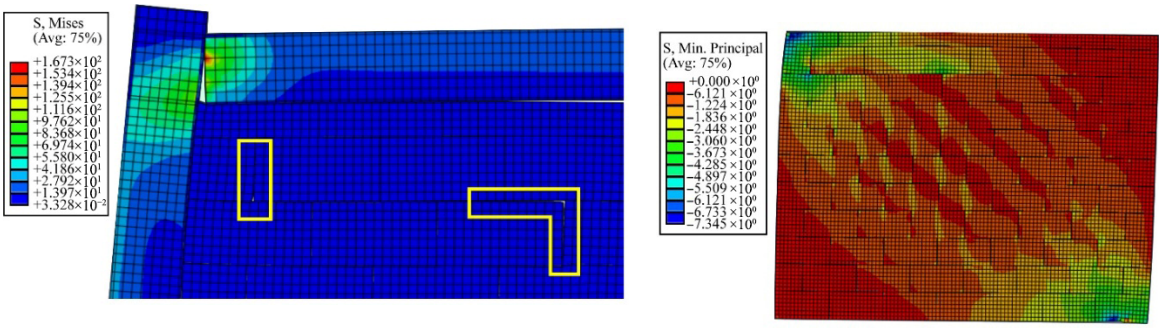
According to Asteris et al. [42], moderate lateral loading induces panel-frame separation due to the stiffness mismatch and subsequent deformation incompatibility between the two components. Contact is maintained exclusively at diagonally opposite corners within the compression zones, where the infill panel effectively acts as an equivalent diagonal strut. This mechanism creates a stress field defined by axial compression along the strut and transverse tensile stresses acting perpendicularly.

These tension and compression struts have been observed in previous numerical studies [68–73]. Labò and Marini [69] identified well-defined diagonal tensile struts, exhibiting maximum plasticization stresses at both corners of the wall. Dhir et al. [68] observed compression and plastic strain distribution rods resulting in brick cracking. Wararuksajja et al. [73] described connecting struts compressed by lateral forces, leading to corner crushing in the compression region. In the masonry numerical simulation by Facconi and Minelli [74], a diagonal crack emerged in the post-cracking stress region, extending from the top left corner to the bottom right corner, with increased damage in the central region.

Under the initial 70 kN load applied to the right, localized separations become apparent between blocks within one horizontal joint and two vertical joints in the upper section of the masonry (Figure 14a). These separations induce disruption in the pre-existing compression rod configuration (Figure 14b). Given the compression strut generated, the masonry presses on both the column and the beam in the upper right corner, which can be verified by the deformation of the block in this corner. There is also a tendency for the beam to detach from the column in the connector region due to the forces generated by the hydraulic actuator and the masonry. Therefore, the connector region operates under tension. This tension is so significant that it counteracts the compression of the blocks on the profiles, promoting the stress distribution shown in Figure 14b.

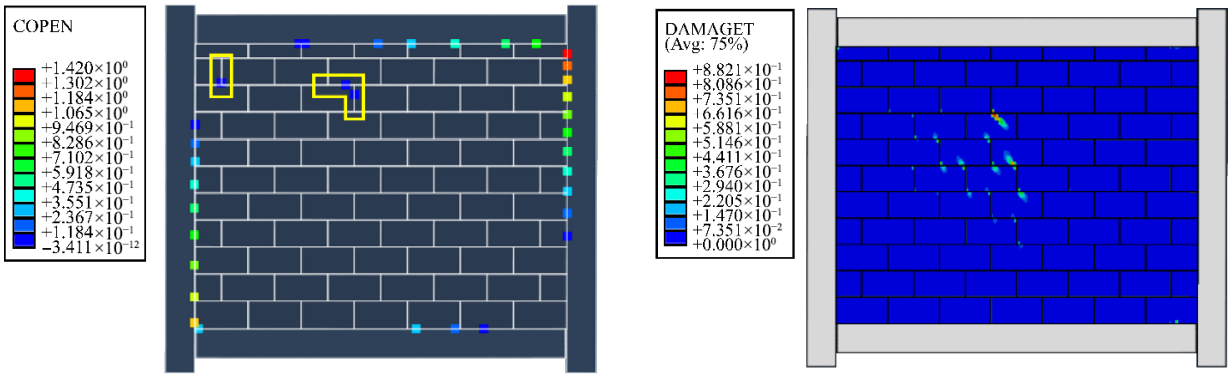
Another method to assess joint opening in ABAQUS software is through the COPEN variable, representing the spacing between surfaces defined with contact conditions. In Figure 15a, areas of the masonry exhibiting the greatest joint openings are highlighted with yellow rectangles. Notably, the separation of the upper horizontal joint is observable, demonstrating the numerical model's capability to predict the precise timing and configuration of the initial crack, consistent with experimental findings. Furthermore, separation between the wall and the steel frame is evident at diagonally opposite uncompressed corners. At this load level (70 kN), damage to the concrete blocks is localized to very specific regions, as illustrated in Figure 15b. These findings are corroborated by the research of Lee, Eom and Yu [72]. When examining the combined impacts of masonry and structure with inferior mortar, they observed separation of the structure wall at tensioned corners within the masonry and block breakage in the connecting strut regions, with pressure concentrated in the central masonry area [72]. Conversely, when poor mortar was not utilized, enhanc-

ing block-structure contact at load-opposite corners, central compression struts formed, alongside corner compression struts in the masonry, resulting in the Push-down effect [72]. This effect caused block failures in both central and corner regions, as well as shear failures in the lower part of the column [72].



(**a**) (**b**)

Figure 14. Displacement of the frame to the left side resulting in (**a**) separation of the units and (**b**) interference with the compression rod (σ_{min}) (displacement magnification: 40×).

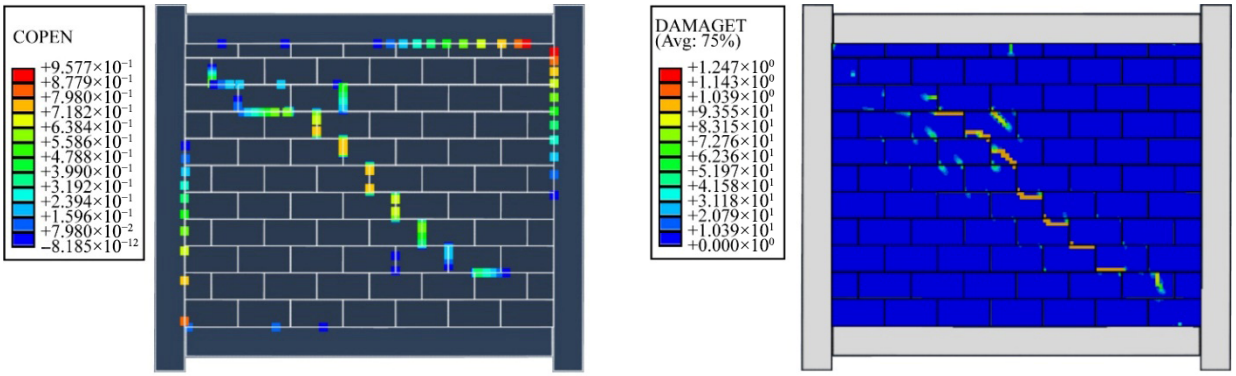


(**a**) (**b**)

Figure 15. Results of applying the first 70 kN load to the right of (**a**) opening in the contacts (COPEN variable), and (**b**) masonry damage (displacement magnification: 1×).

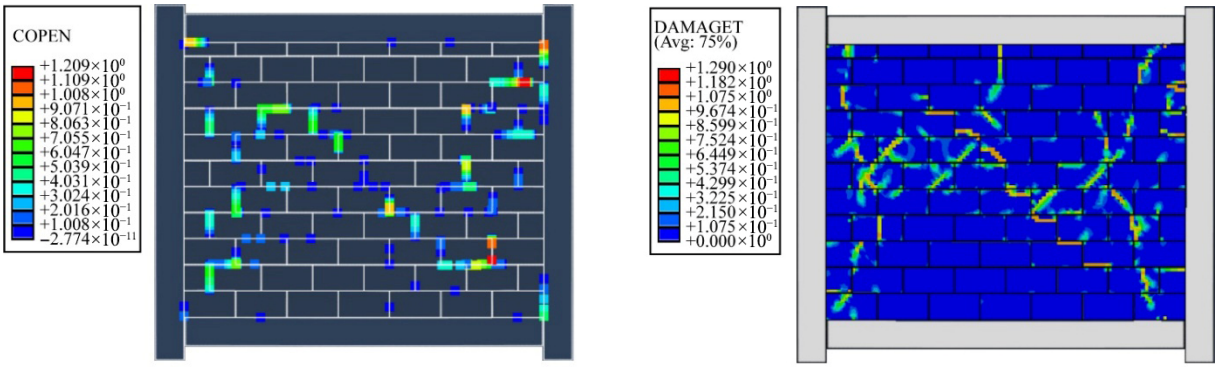
During the second cycle of 70 kN loading, additional regions of separation between the blocks become apparent, forming a staggered pattern diagonally across the masonry, as depicted in Figure 16. This pattern corresponds to a predominance of diagonal tension failure, associated with the lower strength of the mortar relative to the concrete blocks and the poor bond at the block-mortar interface, as explained by De Grandi [41] and Asteris et al. [42]. Furthermore, damage to the blocks is accentuated in more degraded regions near the horizontal joints, particularly in the diagonal panel region. Notably, a similar pattern was observed in the experimental test, but located in the right region of the panel.

In the subsequent loading cycle, a progression of damage occurred along the masonry diagonal depicted in Figure 16, as well as on the opposite diagonal, as shown in Figure 17. This progression aligns with experimental observations. Through analysis of the joint separation pattern and block damage, and load that occurs the first crack between blocks, it is concluded that the numerical model is sufficiently accurate, enabling prediction of the onset of degradation in the involved masonry components.



(**a**) (**b**)

Figure 16. Results after the second load of 70 kN with (**a**) contact spacing (COPEN variable) and (**b**) damage to the blocks (displacement magnification: 1×).



(**a**) (**b**)

Figure 17. Results after all 70 kN cycles with (**a**) contact spacing (COPEN variable) and (**b**) damage to the blocks (displacement magnification: 1×).

The disparities observed between the experimental and numerical results concerning the positioning of contacts exhibiting openings and the levels of block damage can be attributed to the significant heterogeneity and complexity inherent in masonry structures, hindering precise behavioral predictions.

Concrete and mortar have a heterogeneous distribution of grains (aggregates and cement) and voids in different points of the structure. Therefore, predicting the position of a weak zone that will initiate the first rupture is difficult. There is also the influence of the labor force involved in executing the masonry. Since it is a human labor, there will be intrinsic differences between one masonry produced and another, which will be smaller the better the labor force is trained. Asteris et al. [42] discuss these difficulties involved in the study of concrete structures.

Given these challenges, the same experimental test performed with identical frames with concrete masonry may differ slightly in the portion of the joint where the first crack occurs. In fact, in De Grandi's [41] experiments, discrepancies in cracking patterns and corresponding load levels were noted across the three tested frames, despite efforts to maintain consistency in block and mortar batches, joint thickness, and mortar type. Thus, the numerical model PP-E415-050Exp was deemed validated, successfully predicting the onset of masonry degradation and the collapse type.

Furthermore, another advantage of the developed numerical model was its ability to satisfactorily predict the loading-displacement envelope, as illustrated in Figure 18, up

to the point at which the analysis was conducted. The deviations from the experimental values were small (Table 6). Given the asymmetry presented in the experiment, the errors on the tensioned branch were higher in the first cycles. But as the load increased, the errors decreased to a minimum of 0.68% in the tenth load increment. Furthermore, the largest deviations occurred when the displacements were small, below 0.70 mm. At this order of magnitude, any variation in the experimental measurement greatly increases the relative deviation. Thus, the model is considered adequate.

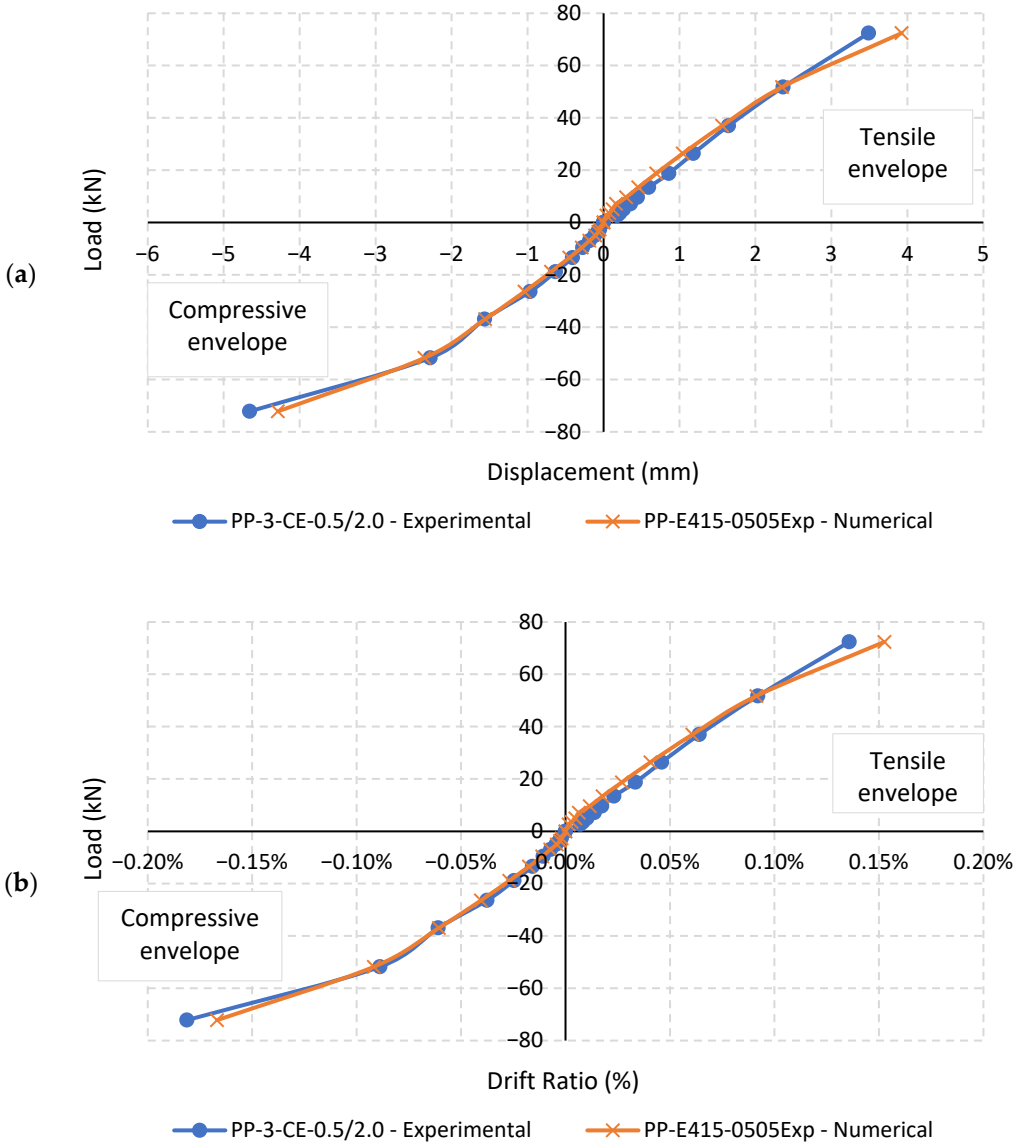


Figure 18. Load envelope obtained by the numerical model: (**a**) displacement (mm) and (**b**) drift ratio (%). Note: The abscissa (**a**) represents the displacements at the top of the frame (corresponding to point RP-13 in the numerical model), while the abscissa (**b**) corresponds to the drift ratio (%). Each '×' and '•' symbol represents the peak load–displacement point of the first cycle for each load step. The sign convention for force and displacement follows the scheme illustrated in Figure 12.

As observed in Table 6, the displacements decrease sharply compared to the empty-frame model, with a maximum drift ratio of 0.17% under a load of 72.17 kN (Figure 18b). For the empty frame, the maximum drift ratio was 1.05% under a load of 51.86 kN (Figure 11c). These results demonstrate the efficiency of masonry as a bracing element.

Table 6. Results obtained experimentally and numerically at each loading step (infilled frame).

Part of Envelope	LOAD STEP	Time (s)	Load (kN)	Displacement (mm)		Drift Ratio (%)		Relative Deviation (%)	Displacement in the Numerical Model
				Experimental	Numerical	Experimental	Numerical		
Compressive	0	0	0	0	0	0.00%	0.00%	0	Equal
	1	29.5	−2.66	−0.05	−0.05	0.00%	0.00%	−0.92	Smaller
	2	56	−3.59	−0.07	−0.07	0.00%	0.00%	−9.05	Smaller
	3	120	−4.97	−0.12	−0.11	0.00%	0.00%	−6.59	Smaller
	4	210.5	−6.95	−0.18	−0.19	−0.01%	−0.01%	−2.60	Bigger
	5	337	−9.58	−0.27	−0.29	−0.01%	−0.01%	−4.60	Bigger
	6	513.5	−13.42	−0.41	−0.45	−0.02%	−0.02%	−10.32	Bigger
	7	760.5	−18.84	−0.63	−0.69	−0.02%	−0.03%	−9.31	Bigger
	8	1107	−26.39	−0.97	−1.04	−0.04%	−0.04%	−7.77	Bigger
	9	1592	−36.91	−1.57	−1.56	−0.06%	−0.06%	−0.46	Smaller
	10	2271.5	−51.75	−2.28	−2.36	−0.09%	−0.09%	−3.30	Bigger
	11	2974	−72.17	−4.66	−4.29	−0.18%	−0.17%	−7.94	Smaller
Tensile	0	0	0	0	0	0.00%	0.00%	0.00	Equal
	1	19.5	2.66	0.18	0.04	0.01%	0.00%	79.23	Smaller
	2	42	3.59	0.21	0.08	0.01%	0.00%	64.49	Smaller
	3	100.5	5.01	0.26	0.12	0.01%	0.00%	54.39	Smaller
	4	181	7.12	0.36	0.17	0.01%	0.01%	53.51	Smaller
	5	299	9.63	0.45	0.30	0.02%	0.01%	33.25	Smaller
	6	460	13.44	0.60	0.46	0.02%	0.02%	23.29	Smaller
	7	685.5	18.77	0.86	0.69	0.03%	0.03%	19.25	Smaller
	8	1001.5	26.4	1.18	1.04	0.05%	0.04%	11.72	Smaller
	9	1444.5	37	1.65	1.56	0.06%	0.06%	5.13	Smaller
	10	2064.5	51.75	2.36	2.35	0.09%	0.09%	0.68	Smaller
	11	2902	72.39	3.49	3.92	0.14%	0.15%	12.42	Bigger

3.3. Comparison Between Experimental Tests and the Numerical Model

Figure 19 displays the envelopes derived from the numerical model developed in this study alongside those from the three frames tested by De Grandi [41]. Despite not extending until the final experimentally applied loading cycle (due to the limitations of the implicit algorithm), the numerical model successfully anticipated the initiation of masonry collapse and accurately represented the load–displacement envelope of the structure, thus affirming its validity.

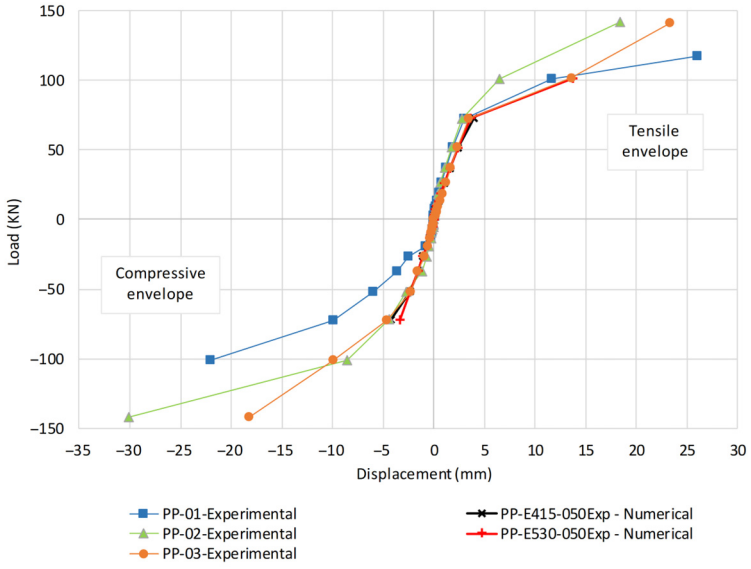


Figure 19. Comparison between the results of the tested frames and the numerical models. Note: The abscissa represents the displacements at the top of the frame (corresponding to point RP-13 in the numerical model), while the ordinate corresponds to the loads applied to the frame. Each '□', 'Δ', '●', '×' and '+' symbol represents the peak load–displacement point of the first cycle for each load step. The sign convention for force and displacement follows the scheme illustrated in Figure 12.

It is noteworthy that although the numerical model was calibrated based on the third frame tested by De Grandi [41], it also effectively represents the behavior observed

in the second test. However, the results of the first tested frame, PP-1-0.5/2.0, notably deviate from the others in terms of the compression curve. De Grandi [41] attributes this discrepancy to the absence of stiffening in the connection angles, unlike the other frames, which likely influences the observed behavioral differences.

For loads exceeding 70 kN, it is evident that experimentally obtained envelopes diverge. This is primarily due to the masonry having reached a significant level of cracking. While there may be a discernible pattern in degradation, it varies from one test to another due to the inherent heterogeneity and complexity of the material, as noted by Asteris et al. [42]. Consequently, depending on the intensity and timing of crack occurrence, the resulting displacement of the filled frame may exceed initial expectations. Regarding the numerical model, at a load of 70 kN, the model has already begun to deal with a high level of cracks. Above 70 kN, the damage to the structure increases significantly, causing the model to fail to converge using the ABAQUS implicit algorithm. However, as the 70 kN load already indicates a loss of masonry efficiency in the bracing of the frame, which means the structure no longer meets its serviceability limit state, it was considered that the numerical model was sufficient. The model effectively predicted the load at which cracks would appear and intensify.

Regarding the stiffness contributed by the participating masonry to the steel frame, a notable difference is observed. In the case of the empty frame, under a load of approximately 50 kN, displacements range from 25 mm to 30 mm. Conversely, in the filled frame, these displacements are approximately 10 times smaller. The study conducted by Kumar and Tripathi [20] further emphasizes the contribution of masonry to frame stability. Their analysis revealed that empty frames, spanning 1 or 2 floors, exhibited increased displacements and lower resistance to lateral loads compared to masonry-filled frames. This underscores the potential of structural masonry panels in reinforcing steel structures, highlighting the substantial improvement in stiffness they provide.

3.4. Effect of Friction Between Masonry and Steel Frame

Friction occurs when two rough surfaces come into contact and tend to slide over each other. The greater the roughness, the greater the friction. Masonry is clearly rough. On the other hand, steel profiles have a smoother appearance due to the production and treatment process. Even so, there is a roughness in the steel that, when in contact with the masonry, will generate friction during the movement of the infilled frame when subjected to load. This friction partially restricts the movement of the surfaces in contact, resulting in less displacement of the frame. In addition, friction contributes to a better distribution of stresses, which minimizes damage to the structure. Therefore, in order to have a behavior that is more faithful to reality, it is important to consider the influence of friction between the steel frame and the masonry.

The influence of friction between the steel frame and the masonry panel on the system's behavior was assessed by comparing the results of the numerical model PP-E415-050Exp with those of a similar model but with a zero-friction coefficient. Figure 20 illustrates that zero friction renders the structure more susceptible to displacement, particularly for loads exceeding 50 kN. Similar findings were noted by Bhaskar, Bhunia and Palchuri [14], where the absence of friction in the blocks led to an overestimation of the maximum lateral displacement in the numerical results by approximately 18.5%.

Additionally, increases in masonry damage and separation between blocks are evident, as depicted in Figures 21 and 22, respectively. In both models, the integrity of the masonry is compromised after the initial 70 kN load to the right. However, in the model accounting for friction, the involvement of the masonry is significantly less extensive and more localized compared to the model where friction is disregarded. Friction ensures better stress

distribution within the masonry, reducing damage and preserving the panel's structural integrity for a longer period.

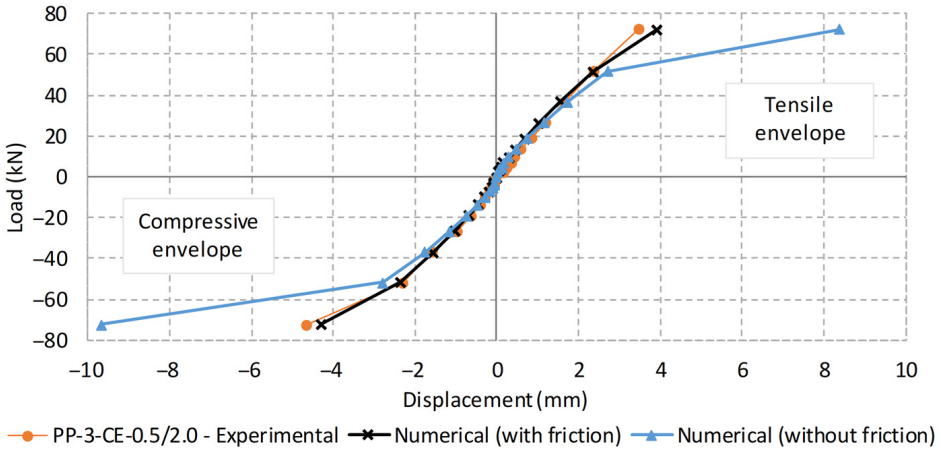
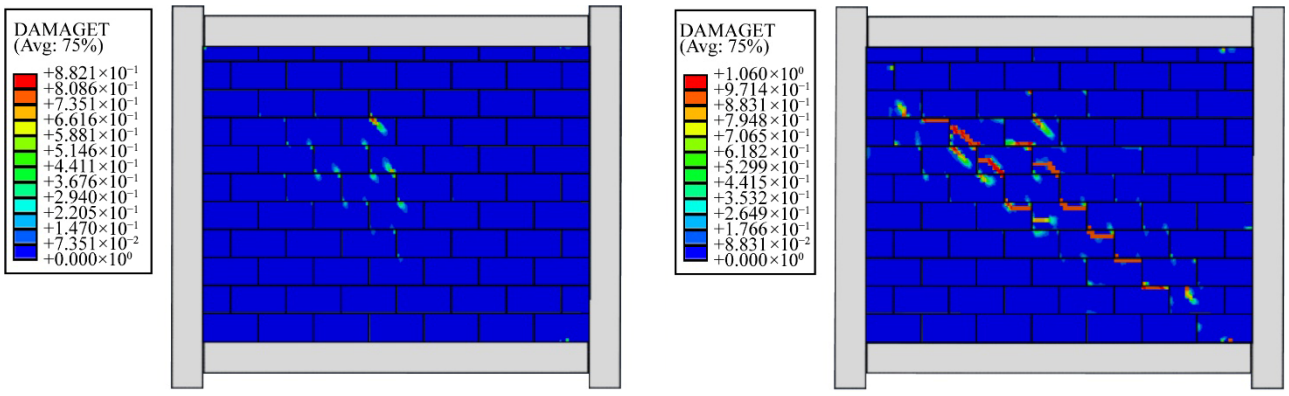
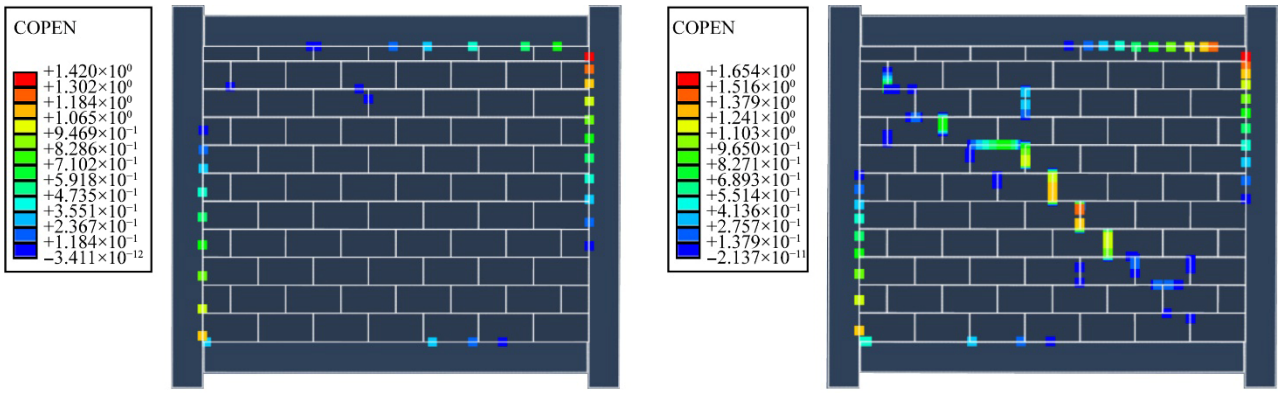


Figure 20. Experimental and numerical envelopes with and without friction.



(**a**) (**b**)

Figure 21. Damage assessed by numerical models (**a**) with friction and (**b**) without friction at the first load of 70 kN to the right (displacement magnification: 1×).



(**a**) (**b**)

Figure 22. Separation between blocks obtained in numerical models (**a**) with friction and (**b**) without friction at the first load of 70 kN to the right (displacement magnification: 1×).

Conversely, when friction is neglected, the stress distribution is impaired, favoring material degradation and unit separation. This process leads to a significant reduction in frame stiffness compared to models that account for frictional effects.

A similar analysis with friction coefficients varying between 0.4, 0.7 and 1.0 was carried out by Liu, Bai and Fu [70], which concluded that the friction force has a low contribution while the mortar resists shear. However, upon reaching maximum shear load, mortar failure occurs, and friction force becomes predominant. A lower coefficient of friction results in block sliding and breakage under lower forces, while a higher coefficient leads to increased block resistance and reduced relative movement, enhancing overall wall displacement resistance before failure. Hence, increased friction enhances wall ductility, supporting greater deformations and resisting higher loads, while decreased friction increases wall fragility [70].

These findings underscore the significant impact of friction between masonry and frame, especially under higher loads. Consequently, contrary to suggestions by Margiacchi et al. [57], neglecting friction simplifications should be avoided. It is essential to thoroughly analyze each case's specific characteristics to ensure an accurate representation of structural behavior.

4. Conclusions

This research has involved the development and validation of numerical models for both empty steel frames and frames filled with structural masonry under cyclic loading conditions. Utilizing the Finite Element Method in ABAQUS software, these models employed simplified micro-modeling techniques to accurately simulate the behavior of masonry components. The main conclusions are summarized as follows:

- The numerical model of the empty frame demonstrated elastic-linear and symmetrical behavior, consistent with theoretical expectations. Minor plasticization occurred during the tension step, resulting in asymmetry in the load–displacement curve. The resulting coefficient of determination (R^2) of 0.977 indicates a strong correspondence between numerical predictions and experimental observations.
- In infilled frames, fracture energy values at interfaces were determined through inverse analysis, 4.15 N/mm for horizontal joints and 0.50 N/mm for vertical joints, with exponential damage evolution. This model accurately predicted the initiation of the first crack in the masonry at a load of 70 kN, anticipating masonry collapse and showing a cracking pattern consistent with experimental observations.
- The numerical load–displacement curve closely matched experimental data, demonstrating the model's reliability. However, the displacement of the filled frame depends on the intensity and timing of crack occurrence, which may exceed initial expectations. The addition of structural masonry greatly increased the stiffness of steel frames, evidenced by displacements under load approximately one-tenth those of empty frames.
- Friction between masonry and steel frames was found to notably affect structural response. Models accounting for a friction coefficient of $\mu = 0.25$ exhibited localized masonry engagement, contrasting with models neglecting friction, which showed increased material degradation, greater unit separation, and reduced frame stiffness. Therefore, the friction parameter must be carefully evaluated in the modeling of infilled frames.
- The simplified model used in this work was able to simulate the complex behavior of infilled frames subjected to cyclic loading. Thus, it is demonstrated that studies in this area can be carried out even with equipment with restrictions in processing power,

which increases the number of researchers who can collaborate with the production of knowledge in the field of masonry and infilled frames.

Based on these findings, incorporating the structural contribution of masonry and a minimum friction coefficient of 0.25 is recommended to optimize frame design. This study confirms that simplified micro-modeling is a reliable, cost-effective tool for performance-based design, providing a validated foundation for scalability to larger or irregular structures, such as high-rise buildings. While this work underscores the efficiency of masonry in bracing steel frames, further research is essential to standardize guidelines for the calculation and construction of these composite systems.

Author Contributions: Conceptualization, R.F.S., J.C.L.R., R.M.d.S. and A.B.C.d.G.; Methodology, R.F.S. and J.C.L.R.; Formal Analysis, R.F.S. and A.M.d.S.; Investigation, R.F.S. and R.R.S.; Writing—Original Draft, R.F.S.; Validation, J.C.L.R., R.M.d.S., L.G.P., A.B.C.d.G. and J.M.F.d.C.; Writing—Review and Editing, J.C.L.R., A.B.C.d.G., R.R.S., A.M.d.S. and J.M.F.d.C.; Supervision, J.C.L.R., R.M.d.S., L.G.P. and J.M.F.d.C.; Project administration, J.C.L.R. All authors have read and agreed to the published version of the manuscript.

Funding: This research was funded in part by the Coordenação de Aperfeiçoamento de Pessoal de Nível Superior—Brazil (CAPES)—Finance Code 001.

Data Availability Statement: The raw data supporting the conclusions of this article will be made available by the authors on request.

Acknowledgments: This research was financed in part by the Coordenação de Aperfeiçoamento de Pessoal de Nível Superior—Brazil (CAPES)—Finance Code 001. The authors also thank the support of the Department of Structural Engineering (UFMG) and the Department of Civil Engineering (UFV). The authors express their gratitude to Rita de Cássia Silva Sant'Ana Alvarenga for the suggestion of the research topic and for the valuable guidance in the early stages of this work.

Conflicts of Interest: The authors declare no conflicts of interest.

Abbreviations

The following abbreviations are used in this manuscript:

CDP	Concrete Damage Plasticity
FEM	Finite Element Method
FEMA	Federal Emergency Management Agency
TVMD	Tuned Viscous Mass Damper

References

1. Parkekian, G.A.; Hamid, A.A.; Drysdale, R.G. *Comportamento e Dimensionamento de Alvenaria Estrutural*, 2nd ed.; EDUFSCAR: São Carlos, Brazil, 2014.
2. Alvarenga, R.D.C.S.S. Theoretical-Experimental Analysis of Steel Frames Infilled with Aerated Autoclaved Concrete Masonry. Ph.D. Thesis, School of Engineering of São Carlos, University of São Paulo, São Carlos, Brazil, 2002.
3. Polyakov, S.V. *Masonry in Framed Buildings*; National Lending Library for Science and Technology: Yorkshire, UK, 1956.
4. Eladly, M.M. Numerical study on masonry-infilled steel frames under vertical and cyclic horizontal loads. *J. Constr. Steel Res.* **2017**, *138*, 308–323. [CrossRef]
5. Dolšek, M.; Fajfar, P. The effect of masonry infills on the seismic response of a four-storey reinforced concrete frame–a deterministic assessment. *Eng. Struct.* **2008**, *30*, 1991–2001. [CrossRef]
6. Yu, Q.Q.; Wu, J.Y.; Gu, X.L.; Wang, L. Seismic behavior of hinged steel frames with masonry infill walls. *J. Build. Eng.* **2023**, *77*, 107536. [CrossRef]
7. Tasnimi, A.A.; Mohebkhah, A. Investigation on the behavior of brick-infilled steel frames with openings, experimental and analytical approaches. *Eng. Struct.* **2011**, *33*, 968–980. [CrossRef]
8. Kappos, A.J.; Ellul, F. Seismic design and performance assessment of masonry infilled r/c frames. In Proceedings of the 12th World Conference on Earthquake Engineering, Auckland, New Zealand, 30 January–4 February 2000; pp. 1–8.

9. Kakaletsis, D.J.; Karayannis, C.G. Influence of Masonry Strength and Openings on Infilled R/C Frames Under Cycling Loading. *J. Earthq. Eng.* **2008**, *12*, 197–221. [CrossRef]
10. Kose, M.M. Parameters affecting the fundamental period of RC buildings with infill walls. *Eng. Struct.* **2009**, *31*, 93–102. [CrossRef]
11. Dawe, J.L.; Seah, C.K.; Liu, Y. A computer model for predicting infilled frame behaviour. *Can. J. Civ. Eng.* **2001**, *28*, 133–148. [CrossRef]
12. Anas, S.M.; Alam, M.; Umair, M. Experimental and numerical investigations on performance of reinforced concrete slabs under explosive-induced air-blast loading: A state-of-the-art review. *Structures* **2021**, *31*, 428–461. [CrossRef]
13. Lee, J.W.; Choi, K.H. Study on the Seismic Performance of Reinforced Concrete Frames with Dry Stack Masonry Wall Using Concrete Block. *Earthq. Struct.* **2023**, *24*, 205–215. [CrossRef]
14. Bhaskar, J.K.; Bhunia, D.; Palchuri, N. Numerical simulation of RC-masonry infill wall system strengthened with textile reinforced concrete. *Mater. Today Proc.* 2023, *in press*. [CrossRef]
15. Srechai, J.; Leelataviwat, S.; Wararuksajja, W.; Limkatanyu, S. Multi-strut and empirical formula-based macro modeling for masonry infilled RC frames. *Eng. Struct.* **2022**, *266*, 114559. [CrossRef]
16. de Sousa, C.; Barros, J.A.O.; Correia, J.R. In-plane cyclic behaviour of RC frames strengthened with composite sandwich panels. *Eng. Struct.* **2022**, *251*, 113529. [CrossRef]
17. Wang, F. Experimental Research on Seismic Performance of Masonry-Infilled RC Frames Retrofitted by Using Fabric-Reinforced Cementitious Matrix Under In-Plane Cyclic Loading. *Int. J. Concr. Struct. Mater.* **2023**, *17*, 31. [CrossRef]
18. Arief, A.; Nurjannah, S.A.; Megantara, Y.; Rusli, M.; Putra, F.E.; Noviyanto, A. Experimental study of confined masonry walls with lap splice reinforcement subjected to cyclic loads. *Eng. Struct.* **2024**, *301*, 117247. [CrossRef]
19. Su, Q.; Cai, G.; Hani, M.; Larbi, A.S.; Tsavdaridis, K.D. Damage control of the masonry infills in RC frames under cyclic loads: A full-scale test study and numerical analyses. *Bull. Earthq. Eng.* **2023**, *21*, 1017–1045. [CrossRef]
20. Kumar, K.H.; Tripathi, R.K. *Damage Assessment of Infilled Frame Structures Using Applied Element Method*; Springer: Dordrecht, The Netherlands, 2024. [CrossRef]
21. Karaka, H.K.; Tripathi, R.K. Assessing potential damage and energy dissipation in low-rise high-strength concrete frames with strong infill walls using applied element method. *Innov. Infrastruct. Solut.* **2023**, *8*, 309. [CrossRef]
22. Nugroho, F.; Maidiawati; Tanjung, J.; Zaidir. Analytical Study on Lateral Strength of Multi-Span Rc Frame with Masonry Infill. *Civ. Environ. Eng.* **2022**, *18*, 448–460. [CrossRef]
23. Alvarenga, R.D.C.S.S.; da Silva, R.M.; Lourenço, P.B.; De Grandi, A.B.C. Numerical-Experimental Evaluation of Masonry Infill Contribution to the Stiffening of Steel Frames. *Rev. Estrut. Aço* **2019**, *7*, 22–39. [CrossRef]
24. Radic, I.; Markulak, D.; Sigmund, V. Analytical modelling of masonry-infilled steel frames. *Teh. Vjesn.–Tech. Gaz.* **2016**, *23*, 115–127. [CrossRef]
25. Ji, X.; Jia, R.; Wang, L.; Wang, M.; Wu, X. Seismic design and performance assessment of a retrofitted building with tuned viscous mass dampers (TVMD). *Eng. Struct.* **2024**, *305*, 117688. [CrossRef]
26. Hou, Y.; Duan, K.; Cao, S.; Liu, J.; Jing, D.; Wang, J. Experimental research on the seismic behavior of brick walls reinforced with dry-connected steel plate frames. *Eng. Struct.* **2023**, *292*, 116586. [CrossRef]
27. De Grandi, A.B.C.; da Silva, R.M.; Alvarenga, R.D.C.S.S.; Ribeiro, J.C.L.; Parsekian, G.A.; Medeiros, W.A. Theoretical analysis of the behavior of steel frame infilled with masonry walls by the diagonal strut method. *Rev. IBRACON Estrut. Mater.* **2021**, *14*, e14508. [CrossRef]
28. Markulak, D.; Dokšanović, T.; Radić, I.; Zovkić, J. Behaviour of steel frames infilled with environmentally and structurally favourable masonry units. *Eng. Struct.* **2020**, *204*, 109909. [CrossRef]
29. Gorji Azandariani, M.; Mohebkhah, A. A multi-strut model for the hysteresis behavior and strength assessment of masonry-infilled steel frames with openings under in-plane lateral loading. *Eng. Struct.* **2024**, *302*, 117433. [CrossRef]
30. Song, X.; Lu, Y.; Zhang, B.; Chen, X. Seismic behavior of damaged Li-Tie style timber frames with brick masonry infills: Experimental test, finite element analyses, and behavior degradation. *J. Build. Eng.* **2024**, *86*, 108848. [CrossRef]
31. Anas, S.M.; Shariq, M.; Alam, M.; Umair, M. Modeling of crashworthy foam mounted braced unreinforced brick masonry wall and prediction of anti-blast performance. *Int. J. Prot. Struct.* **2024**, *15*, 241–283. [CrossRef]
32. Lagomarsino, S.; Penna, A.; Galasco, A.; Cattari, S. TREMURI program: An equivalent frame model for the nonlinear seismic analysis of masonry buildings. *Eng. Struct.* **2013**, *56*, 1787–1799. [CrossRef]
33. Rozylo, P. Comparison of Failure for Thin-Walled Composite Columns. *Materials* **2021**, *15*, 167. [CrossRef]
34. Rozylo, P.; Debski, H. Stability and load-carrying capacity of short composite Z-profiles under eccentric compression. *Thin-Walled Struct.* **2020**, *157*, 107019. [CrossRef]
35. Rozylo, P. Failure phenomenon of compressed thin-walled composite columns with top-hat cross-section for three laminate lay-ups. *Compos. Struct.* **2023**, *304*, 116381. [CrossRef]
36. Doudoumis, I.N. Finite element modelling and investigation of the behaviour of elastic infilled frames under monotonic loading. *Eng. Struct.* **2007**, *29*, 1004–1024. [CrossRef]

37. Radnić, J.; Baloević, G.; Matešan, D.; Smilović, M. On a numerical model for static and dynamic analysis of in-plane masonry infilled steel frames. *Mater. Werkst.* **2013**, *44*, 423–430. [CrossRef]
38. Damiani, N.; DeJong, M.J.; Albanesi, L.; Graziotti, F.; Morandi, P. Parametric study on the in-plane performance of a steel frame retrofit solution for URM buildings using DEM. *Eng. Struct.* **2024**, *302*, 117293. [CrossRef]
39. Chen, D.; Wu, H.; Xu, S.; Wei, J. Shock tube tests and dynamic behavior analyses on one-way masonry-infilled walls. *Baozha Yu Chongji/Explos. Shock. Waves* **2023**, *43*, 085103. [CrossRef]
40. Asgarkhani, N.; Kazemi, F.; Jankowski, R.; Formisano, A. Dynamic ensemble-learning model for seismic risk assessment of masonry infilled steel structures incorporating soil-foundation-structure interaction. *Reliab. Eng. Syst. Saf.* **2026**, *267*, 111839. [CrossRef]
41. De Grandi, A.B.C. Experimental Evaluation by Cyclic Testing of Steel Frame Infilled with Masonry Walls. Master's Thesis, Universidade Federal de Viçosa, Viçosa, Brazil, 2018.
42. Asteris, P.G.; Kakaletsis, D.J.; Chrysostomou, C.Z.; Smyrou, E.E. Failure Modes of In-filled Frames. *Electron. J. Struct. Eng.* **2011**, *11*, 11–20. [CrossRef]
43. Arslan, M.E.; Aykanat, B.; Subaşı, S.; Maraşlı, M. Cyclic behavior of autoclaved aerated concrete block infill walls strengthened by basalt and glass fiber composites. *Eng. Struct.* **2021**, *240*, 112431. [CrossRef]
44. Tso, W.K.; Rutenberg, A.; Heidebrecht, A.C. Cyclic Loading of Externally Reinforced Masonry Walls Confined by frames. *Can. J. Civ. Eng.* **1975**, *2*, 489–493. [CrossRef]
45. Wang, X.; Li, F.; Wan, L.; Li, T. Hysteretic performance of a novel composite wall panel consisted of a light-steel frame and aerated concrete blocks. *Steel Compos. Struct.* **2021**, *41*, 861–871. [CrossRef]
46. Játiva, J.; Torres, I.; Hernández, L.; Arévalo, D. Study of the Reinforcement of Concrete Block Masonry through Destructive Tests Applied to Steel Frames with Bolted Joints. *Rev. Politec.* **2023**, *51*, 87–97.
47. Weaver, W.; Johnston, P.R.; Douglas, A.S. Finite Elements for Structural Analysis. *J. Appl. Mech.* **1984**, *51*, 705. [CrossRef]
48. Lourenço, P.J.B.B. *Computational Strategies for Masonry Structures*; Delft University Press: Delft, The Netherlands, 1996.
49. Santos, C.F.R.; Alvarenga, R.C.S.S.; Ribeiro, J.C.L.; Castro, L.O.; Silva, R.M.; Santos, A.A.R.; Nalon, G.H. Numerical and experimental evaluation of masonry prisms by finite element method. *Rev. IBRACON Estrut. Mater.* **2017**, *10*, 477–508. [CrossRef]
50. Bolhassani, M.; Hamid, A.A.; Lau, A.C.W.; Moon, F. Simplified micro modeling of partially grouted masonry assemblages. *Constr. Build. Mater.* **2015**, *83*, 159–173. [CrossRef]
51. Bolhassani, M.; Hamid, A.A.; Johnson, C.; Moon, F.L.; Schultz, A.E. New Design Detail to Enhance the Seismic Performance of Ordinary Reinforced Partially Grouted Masonry Structures. *J. Struct. Eng.* **2016**, *142*, 04016142. [CrossRef]
52. Simulia. *Abaqus/CAE User's Manual*, Version 6.12; Dassault Systèmes: Providence, RI, USA, 2012. Available online: http://orpheus.nchc.org.tw:2080/v6.12/books/usb/default.htm (accessed on 2 February 2026).
53. El-Khoriby, S.; Sakr, M.A.; Khalifa, T.M.; Eladly, M.M. Modelling and behaviour of beam-to-column connections under axial force and cyclic bending. *J. Constr. Steel Res.* **2017**, *129*, 171–184. [CrossRef]
54. ABNT, NBR 6118; Projeto de Estruturas de Concreto—Procedimento. 2023. Available online: https://ikigai.eco.br/download/nbr-6118.pdf (accessed on 2 February 2026).
55. Mohebkhah, A.; Tasnimi, A.A.; Moghadam, H.A. Nonlinear analysis of masonry-infilled steel frames with openings using discrete element method. *J. Constr. Steel Res.* **2008**, *64*, 1463–1472. [CrossRef]
56. Sarhosis, V.; Tsavdaridis, K.D.; Giannopoulos, I. Discrete Element Modelling of Masonry Infilled Steel Frames with Multiple Window Openings Subjected to Lateral Load Variations. *Open Constr. Build. Technol. J.* **2014**, *8*, 93–103. [CrossRef]
57. Margiacchi, F.; Salvatori, L.; Orlando, M.; De Stefano, M.; Spinelli, P. Seismic response of masonry-infilled steel frames via multi-scale finite-element analyses. *Bull. Earthq. Eng.* **2016**, *14*, 3529–3546. [CrossRef]
58. Fonseca, G.M. *Análise Numérico Experimental da Interação Conjunta Pórtico-Alvenaria*; Universidade Federal de Minas Gerais: Minas Gerais, Brazil, 1999.
59. Byfield, M.P.; Dhanalakshmi, M. Analysis of strain hardening in steel beams using mill tests. In *Advances in Steel Structures (ICASS '02)*; Chen, W.F., Teng, J.G., Eds.; Elsevier: Amsterdam, The Netherlands, 2002; pp. 139–146. [CrossRef]
60. Guo, Z. *Principles of Reinforced Concrete*; Elsevier: Amsterdam, The Netherlands, 2014. [CrossRef]
61. Dutra, C.M. *Estudo do Comportamento Estrutural do Conector Crestbond Considerando Variações Geométricas e Mecânicas*; Universidade Federal de Viçosa: Minas Gerais, Brazil, 2014.
62. Hordijk, D.A. *Local Approach to Fatigue of Concrete*; Delft University of Technology: Delft, The Netherlands, 1991.
63. Federação Internacional do Betão (FIB). *Model Code 2010–Final Draft, fib*; The International Federation for Structural Concrete: Lausanne, Switzerland, 2012. [CrossRef]
64. Federal Emergency Management Agency. *FEMA 461—Interim Testing Protocols for Determining the Seismic Performance Characteristics of Structural and Nonstructural Components*; EUA: Redwood City, CA, USA, 2007.
65. Faleschini, F.; Hofer, L.; Zanini, M.A.; dalla Benetta, M.; Pellegrino, C. Experimental behavior of beam-column joints made with EAF concrete under cyclic loading. *Eng. Struct.* **2017**, *139*, 81–95. [CrossRef]

66. Kawecki, B.; Podgórski, J. Numerical Results Quality in Dependence on Abaqus Plane Stress Elements Type in Big Displacements Compression Test. *Appl. Comput. Sci.* **2017**, *13*, 56–64. [CrossRef]
67. Smith, B.S. Lateral Stiffness of Infilled Frames. *J. Struct. Div.* **1962**, *88*, 183–199. [CrossRef]
68. Dhir, P.K.; Tubaldi, E.; Ahmadi, H.; Gough, J. Numerical modelling of reinforced concrete frames with masonry infills and rubber joints. *Eng. Struct.* **2021**, *246*, 112833. [CrossRef]
69. Labò, S.; Marini, A. In-plane flexural behavior of hollow brick masonry walls with horizontal holes. *Eng. Struct.* **2022**, *273*, 115086. [CrossRef]
70. Liu, B.; Bai, G.L.; Fu, G.M. *Seismic Performance and Reinforcement Strategy of Frame Infilled with ESPS Block Masonry Wall: Experimental, Theoretical and Numerical Investigation*; Springer: Dordrecht, The Netherlands, 2022. [CrossRef]
71. Mohammad, A.F.; Khalid, F.; Khan, R.A. Finite element micro-modelling of RC frames with variant configurations of infill masonry. *Struct. Eng. Mech.* **2022**, *81*, 395–409. [CrossRef]
72. Lee, S.J.; Eom, T.S.; Yu, E. Investigation of Diagonal Strut Actions in Masonry-Infilled Reinforced Concrete Frames. *Int. J. Concr. Struct. Mater.* **2021**, *15*, 6. [CrossRef]
73. Wararuksajja, W.; Srechai, J.; Leelataviwat, S.; Sungkamongkol, T.; Limkatanyu, S. Seismic design method for preventing column shear failure in reinforced concrete frames with infill walls. *J. Build. Eng.* **2021**, *44*, 102963. [CrossRef]
74. Facconi, L.; Minelli, F. Retrofitting RC infills by a glass fiber mesh reinforced overlay and steel dowels: Experimental and numerical study. *Constr. Build. Mater.* **2020**, *231*, 117133. [CrossRef]

Disclaimer/Publisher's Note: The statements, opinions and data contained in all publications are solely those of the individual author(s) and contributor(s) and not of MDPI and/or the editor(s). MDPI and/or the editor(s) disclaim responsibility for any injury to people or property resulting from any ideas, methods, instructions or products referred to in the content.